

Numerical Modeling of Gas in Spiral Arms with a Simplified HI Cooling Function

A Second Year Project

Meredith McCarthy¹

Advisor: Eve Ostriker

Committee members: Stuart Vogel, Mark Wolfire

1. Introduction

The structure and dynamical evolution of the spiral arms of galaxies are characterized by the competing processes of gravity, shocks, magnetic fields, mass transport, and heating and cooling. By studying the interplay between these forces, the time evolution and overall structure of spiral arms can be characterized. Recent advances in magnetohydrodynamic simulation of the interstellar medium enable more realistic study of the influences from each relevant process, with the goal of reconciling numerical results with observed properties of spiral arms.

In particular, the treatment of gas interaction in spiral shocks has been previously limited by numerical algorithms and computational restraints. Also, while the overall theory of a multiphase ISM has existed since the early two phase model of Field, Goldsmith, & Habing (1969) and since evolved into a three phase model (Cox & Smith 1974; McKee & Ostriker 1977; Spitzer 1978), there still exists a lack of detailed understanding regarding the intricate interactions between the phases. This has led to discrepancies in observed spiral arm profiles and calculated ones.

Development of gaseous spiral arm modeling extends back to the first one dimensional steady state models which studied gas flow subject to spiral gravitational field forcing (Roberts 1969; Shu et al. 1973). The Roberts model showed for the first time that shocks form. Roberts argued that the increased surface density and reduction of shear caused by spiral shocks encourages gas condensation and star formation in the peak and immediately trailing edges of the shock. The Shu et al. (1973) models focused on linking the breadth of arms to the sound speed of the flowing gas, and studied simple substructures due to resonances in the arms. These models, which adopted an isothermal equation of state, produced the classical sharp discontinuity at the shock, with slow postshock decline for the spiral density profile. However, these models lacked any treatment of the gas as a multiphase component and lacked the time dependence of the spiral shock. Time evolution was first studied by Woodward (1974), who showed how shocks form in a spiral potential through convective steepening. However, this model was still for a single phase medium.

¹Department of Astronomy, University of Maryland, College Park, MD 20740

Further refinements in modeling shocks in spiral arms came in the mid to late 80s with the inclusion of a pseudo-cloudy medium (Balbus & Cowie 1985; Lubow, Balbus, & Cowie 1986; Balbus 1988a,b). These analyses used idealized approaches to treating a gas consisting of a collection of discrete, interacting, cold cloudlets. Mathematically, the hydrodynamic equations were modified to include an explicit, bulk viscosity. Their intent with this approach was to model a multiphase medium with an effective diffusion associated with large mean free paths for cloud collisions. In these models, the spiral arm profiles became smoother as the viscosity was increased. By studying the growth of self-gravitating perturbations in the linear regime, they suggest that arm substructures form due to transient gravitational instabilities. With self-gravity, an increase of the gas fraction had the effect of smoothing out the shock profile and shifting its peak, while low gas fractions produced a more saw-toothed shock profile.

The interaction of gas with spiral shocks has also been modeled with N-body simulations which treats the gas as individual sticky particle clouds (Schwarz 1981; Combes & Gerin 1985). This treatment of the ISM would seem to capture some properties of a realistic gas distribution when most of the material is in small cold clouds. The actual implementation requires parameterizing the clouds with ad hoc equations for energy exchange and collisions. This method has thus far been unable to resolve sharp features such as sudden velocity jumps and strong density gradients.

Recently, gas in spiral shocks has been modeled using hydrodynamical codes, which are able to model the time dependent evolution of the gas by solving standard fluid equations. These methods are able to faithfully reproduce observed gas kinematics of spirals (Regan, Vogel, & Teuben 1997; Regan, Sheth, & Vogel 1999). While a wide range of work has been done using this method, most significant to this study is the work of Kim & Ostriker (2002), hereafter KO02. They modeled the gas in a rigidly rotating spiral potential as differentially rotating, razor thin disks with self-gravity and magnetic fields. These nonlinear two dimensional simulations produced the spur-like structures seen in many spiral galaxies. However, the gas was treated as an isothermal fluid. Other approaches include treatment of the gas via smoothed particle hydrodynamics (Gittins, Clarke, & Bate 2003; Gittins & Clarke 2004), where interacting gas cloudlets are observed to collide, merge, and gravitationally collapse in a spiral potential.

At this juncture, we still lack simulations of a realistic cloudy medium interacting with a spiral gravitational potential. What effect would a non-isothermal treatment of the gas have on the overall structure of spiral shocks? In particular, are more realistic simulations able to reproduce the observed average profiles of the gas in spiral galaxies? These observed profiles are more symmetric than those produced by isothermal models (Shetty et al. 2005), as shown in Figure 4. Is the average profile smoother when cloudy structure is incorporated, as is possible in simulations that include a realistic HI cooling function?

With these questions in mind, this work seeks to improve upon previous studies by adding a more realistic treatment of gas cooling and heating mechanisms. We simulate via MHD the time evolution of a differentially rotating cloudy medium in a rigidly rotating spiral potential. The gas

is treated as a razor thin disk in the plane of the arm. Instead of using isothermal cooling, we include a simplified cooling function which closely follows that of a realistic two-phase ISM. Both one and two dimensional cases are considered.

The remainder of the paper will proceed as follows. In Section 2.1, we outline the MHD equations used for the simulations. We then discuss the cooling function and its implementation in Section 2.2, followed by a summary of the numerical method used and its validation in Sections 2.3 and 2.4. Section 3 contains detailed descriptions of the parameters studied in this paper, and then details the variety of simulations performed and analyzed. Finally, Section 4 summarizes our chief conclusions.

2. Methods

2.1. Model Equations

We study a magnetized, differentially rotating, razor thin gaseous disk in an externally imposed spiral potential, with optically thin heating and cooling. Following KO02, the spiral potential arises from the stellar component of a spiral arm, which is assumed to be tightly wound and rigidly rotating with a constant pattern speed Ω_p relative to the inertial frame. The radial velocities resultant from the noncircular motion of the spiral forcing cause nonlinearly compressed spiral arms.

A Cartesian frame is constructed based on the work of Roberts (1969). In this model, the center of the local frame is at R_0 and it rotates at the pattern speed Ω_p about this center. The two coordinates with respect to this moving frame are then the radial displacement ($R - R_0$) and the angular displacement ($R_0(\theta - \Omega_p t)$). A local rectangular box is recovered by tilting the entire frame at an angle i such that the x and y directions correspond to the direction perpendicular and parallel to the spiral arm, respectively. The dimensions of the box are L_x and L_y .

The time-dependent equations of MHD are expanded into this rotating frame with the following approximations from KO02. Spiral arms are assumed to be tightly wound, such that the pitch angle $i = \arctan(\lambda_R/\lambda_\theta) \ll 1$. A local model insists that $L_x, L_y \ll R_0$, and the arm induced velocities are much smaller than ΩR_0 . Volumetric heating and cooling terms, and a thermal conduction term, are then included in the MHD equations to yield the following (in standard notation):

$$\frac{\partial \rho}{\partial t} + \nabla \cdot (\rho \mathbf{v}) = 0, \quad (1)$$

$$\frac{\partial \mathbf{v}}{\partial t} + \mathbf{v} \cdot \nabla \mathbf{v} = -\frac{\nabla \mathbf{P}}{\rho} + \frac{1}{4\pi\rho}(\nabla \times \mathbf{B}) \times \mathbf{B} + 2q\Omega^2 \mathbf{x} \hat{\mathbf{x}} - 2\Omega \times \mathbf{v}, \quad (2)$$

$$\frac{\partial \mathcal{E}}{\partial t} + \mathbf{v} \cdot \nabla \mathcal{E} = -(\mathcal{E} + P)\nabla \cdot \mathbf{v} - \rho \mathcal{L} + \nabla \cdot (\mathcal{K} \nabla T) \quad (3)$$

$$\frac{\partial \mathbf{B}}{\partial t} = \nabla \times (\mathbf{v} \times \mathbf{B}). \quad (4)$$

Here,

$$q = \frac{-d\ln\Omega}{d\ln R} \rightarrow 1 \quad (5)$$

for a flat rotation curve.

2.2. Cooling

The net cooling per mass is given by

$$\mathcal{L} = \rho\Lambda(\rho, T) - \Gamma \quad (6)$$

We implemented a simplified cooling function based on detailed cooling parameter tables provided by Mark Wolfire (Wolfire et al. 1995, 2003). These tables give the value of net heating and cooling due to the principle ISM processes, including: photoelectric heating from small grains and PAHs, X-ray heating, cosmic ray heating, CI photoionization heating, fine structure cooling of C II, OI, and CI, Lyman alpha transition cooling, and cooling due to recombination onto grains. The parameter space is $5.0 \text{ K} < T < 2 \times 10^4 \text{ K}$ by $10^{-2} \text{ cm}^{-3} < n < 10^3 \text{ cm}^{-3}$. The values are defined for solar metallicity and a shielding column of $N = 10^{19} \text{ cm}^{-2}$, which corresponds to a warm neutral medium cloud of about $1 M_\odot$. This is the expected WNM cloud size in a three phase ISM (McKee & Ostriker 1977). All calculations of \mathcal{L} are made using a calculation for the X-ray/Extreme UV flux with the same average column density as above (Wolfire et al. 1995, 2003).

Figure 2 shows the contours of \mathcal{L} as a function of the thermal pressure P/k and hydrogen density n . The equilibrium curve is denoted by the 0 curve. Gas in the region above the curve has net cooling ($\mathcal{L} > 0$) and gas below the curve has net heating ($\mathcal{L} < 0$). Cold or warm phase gas will respond to perturbations in temperature by either cooling or heating back to the equilibrium curve. As originally detailed in Field, Goldsmith, & Habing (1969), the local shape of the cooling curves determines the stability of the perturbed media, thus characterizing the process of thermal instability. For isobaric cooling, gas is thermally stable where $d(\log P)/d(\log n) > 0$ and thermally unstable where $d(\log P)/d(\log n) < 0$ on the equilibrium curve. Perturbed gas in the thermally unstable region will either continue to heat or cool in the same direction as the temperature gradient of its original perturbation until it reaches one of the other two equilibrium points.

A simple cooling function fit to the Wolfire et al. (1995) cooling tables is described in Sánchez-Salcedo et al. (2002). We follow Piontek & Ostriker (2004), hereafter PO04, in implementing this function as a close approximation to the cooling of a cloudy medium. The function consists of a

piecewise exponential function a defined as follows:

$$\Lambda = C_{i,i+1} T^{\beta_{i,i+1}} \text{ for } T_i \leq T \leq T_{i+1} \quad (7)$$

where the values of β are $\beta_{12} = 2.13$, $\beta_{23} = 1.0$, $\beta_{34} = 0.56$ and $\beta_{45} = 3.67$ and the corresponding critical T values are $T_1 = 10 \text{ K}$, $T_2 = 141 \text{ K}$, $T_3 = 313 \text{ K}$, $T_4 = 6102 \text{ K}$ and $T_5 = 10^5 \text{ K}$. C is given in $\text{ergs s}^{-1} g^{-2} K^{-\beta_{i,i+1}}$ by $C_{1,2} = 3.42 \times 10^{16}$, $C_{2,3} = 9.10 \times 10^{18}$, $C_{3,4} = 1.11 \times 10^{20}$, and $C_{4,5} = 2.00 \times 10^8$ assuming constant heating, Γ . This assumption is made based on the weak density dependence ($\rho^{0.2}$) of the heating term when the dominant heating term is due to photoelectric heating from small grains and PAHs. Thus $\Gamma = 0.015 \text{ ergs s}^{-1} g^{-1}$.

Figure 3 displays contours of the simplified cooling function at the same levels as were shown in Figure 2 for the full cooling tables. The fit appears to match well although the detailed cooling function seems to be shifted upwards by a small factor.

2.3. Code and Numerical Methods

The time dependent evolution of the MHD equations is integrated with a version of the ZEUS-2D code (Stone & Norman 1992a,b). ZEUS implements a time-explicit, operator-split, finite differencing method for solving MHD on a staggered mesh. On this mesh, velocities and magnetic fields are face-centered, while energy and mass density are volume-centered quantities. Accurate propagation of Alfvén waves is ensured by the method of characteristics, while $\nabla \cdot \mathbf{B}$ is maintained within machine accuracy by constrained transport (Evans & Hawley 1988; Hawley & Stone 1995).

For this study, a hybrid version of the ZEUS code has been created from the previous works of Kim & Ostriker (2002) and Piontek & Ostriker (2004). Following the former, the simulations are two dimensional in the x-y plane. Our box has shearing box boundary conditions, where x boundaries are shearing periodic while y-boundaries are purely periodic. The velocity decomposition method of Kim & Ostriker (2001) is employed to minimize diffusion from advection due to the background shear.

As in PO04, cooling is solved implicitly using the Newton-Raphson method. This method is chosen since cooling times can be much shorter than dynamical times, making detailed time step control necessary. The timestep is reduced by a factor of two if any zone on the grid changes in temperature by more than a factor of 10%. In order to have realistic amplitudes for external spiral potential before cooling is initialized, we first run with an isothermal equation of state for three orbits, with a gradual initialization of the external potential to its full value by the second orbit. The variability of the isothermal case over three orbits will be discussed in section 3.2. Only after the arm density profile is steady do we turn on the cooling with an ideal gas law parameterized by $\gamma = 5/3$, where γ is the heat capacity ratio c_p/c_v for monoatomic gases.

2.4. Code Tests

The ZEUS code itself is a well established and has been thoroughly tested in a wide variety of astronomical problems. The implementation of the external potential and the cooling functions has also been established and tested, and those results can be found in KO02 and PO04 respectively.

The hybrid code was tested on a variety of simple cases for validation. The code can produce long lived isothermal spiral shocks with little variation in amplitude. A secondary density perturbation forms occasionally due to the superharmonic resonance of the arm; this is a result of not having self gravity within the simulations (see KO02). We do not include self gravity here, however, as it would lead to large-scale, gravitationally bound clouds rather than a system of smaller clouddlets more characteristic of the atomic ISM. The hybrid code is also able to reproduce the thermal instability results of PO04.

2.5. Visualization

In addition to modifications in ZEUS, a large package of IDL routines was created to facilitate improved visualization and analysis of the ZEUS data. The final products can plot static images from HDF dumps or produce movies of the data with a great deal of versatility. Static plots image density, energy, temperature, velocities, and/or magnetic fields with the option of vector field or contour overlays. Density profiles can also be plotted of both 1D and 2D simulations. Other original routines can produce movies of any of the above parameters. All of these tools will be included in any local distribution of the ZEUS code.

3. Simulations

3.1. Relevant Parameters

We present a variety of one and two dimensional simulations of gaseous spiral arm development with a simplified cooling function. The two dimensional cases are at 256x256 resolution with physical dimensions of 1 kpc in both x and y . The one dimensional cases are at a resolution of 1280x2, with the x physical dimension of 1kpc. These dimensions were chosen in order to maintain a reasonable physical size for clouds close to the Spitzer standard size for HI clouds (1-10pc). Although a more reasonable physical scale for spiral arm periodicity is 3kpc, the increase in resolution by a factor of three would be too computationally intensive for the available resources. We suggest that the 1 kpc box size models will qualitatively represent the main effects that results, independent of size.

The initial density and pressure are chosen to be representative of diffuse ISM. Thus the density is $n = 1 \text{ cm}^{-3}$ with an initial $P/k = 2000 \text{ K cm}^{-3}$. Constant parameters include the

heating term and \mathcal{K} , the magnitude of the conduction term. Conduction is important in thermal instability simulations in preventing unresolved growth of perturbations. Our \mathcal{K} was chosen to be $2.575 \times 10^8 \text{ ergs cm}^{-1}$ for the 2d case and $1.609 \times 10^7 \text{ ergs cm}^{-1}$ for the 1D case, such that the field length for thermal instability is resolved by 8 grid zones (Piontek & Ostriker 2004).

The overall timescale is six orbits. The first two orbits are isothermal and are characterized by the gradual establishment of a background spiral gravitational potential defined by an amplitude ε , defined as:

$$\varepsilon = \frac{2\pi}{\lambda} \frac{\Phi_{ext}}{\Omega_0^2 R_0} \quad (8)$$

Amplitudes are chosen so that the contrast between background conditions and the spiral arm lie between a factor of a few and ten. The parameter ε ranges between 0.02 and 0.05 for the 1D cases and held constant at 0.035 for the 2D cases. The third orbit consists of the full established spiral potential with purely isothermal gas; this orbit allows the potential to settle before being shocked by cooling. Cooling is turned on after the third orbit and thermal instability is allowed to progress freely.

A variety of magnetic fields strengths are applied to the 1D and 2D cases, characterized by an amplitude β ,

$$\beta = \frac{2c_s^2}{v_A^2} = \frac{4\pi\rho_0 c_s^2}{B^2} \quad (9)$$

where v_A is the Alfvén speed. The range of values is $1 \leq \beta \leq 100$, where $\beta = 1 - 10$ are typical values for interstellar magnetic fields. The corresponding mean magnetic field strength is then

$$B = \frac{3.2}{\sqrt{\beta}} \mu G \left(\frac{n_H}{1 \text{ cm}^{-3}} \right)^{1/2} \left(\frac{c_s}{7.0 \text{ km s}^{-1}} \right) \quad (10)$$

Table 1 contains a summary of the simulations that will be discussed for the remainder of this section.

3.2. Isothermal Stability

As described in the Methods section, cooling turned on after three orbits. This is in order to give the underlying spiral arm potential enough time to achieve a steady gas profile. Previously, Kim & Ostriker (2002) found that a uniform initial density background with a gradually imposed external spiral potential reached a steady state after 5 orbits. We conclude that for the simple cases run for this paper, three orbits is adequate.

Figure 4 shows samples of the overall time evolution of the isothermal shock for the case of $\varepsilon = 0.035$. These profiles, as are all subsequent profiles unless explicitly stated, are boxcar smoothed over 10 pcs. For the simulations studied here, this corresponds to 3 zones for the 256x256 resolution simulations and 10 zones for the 1024x2 simulations.

Examining Figure 4, typical flat-faced shock front produced by a spiral external potential in an isothermal medium is immediately obvious. The secondary density perturbation that forms periodically on the trailing end of the shock is caused by the ultraharmonic resonance (Shu et al. 1973). The amplitude and variability of the shock front settles near the third orbit.

This stability after three orbits is better seen in the next series of images, which shows a host of 1D simulations at a range of ε (see Figs. 5, 6, 7, 9, and 10) and a 2D case at $\varepsilon=0.035$ for comparison (Fig. 8). The overlays are different snapshots of the average profile of the simulation at times following the third orbit. Lower values of ε converge less convincingly to a steady state, while $\varepsilon=0.035$ is the weakest potential to have a consistent profile over time. Thus $\varepsilon=0.035$ is chosen as the amplitude of the external potential to study the two dimensional evolution of a cooled spiral shock. While we could have chosen a larger value, we want to minimize the density contrast between the background and the spiral arm.

It is also significant that there is no obvious difference between the 2D and 1D isothermal cases at $\varepsilon=0.035$ (Figs. 7, 8). Most likely, the 2D potential would settle more quickly than the 1D given its extra degree of freedom. Regardless, we shall maintain a 3 orbit turn-on time for the cooling so that comparisons can be easily made between the low and high resolution cases.

3.3. 2D Time Evolution

The 2D density images for the four cases of no magnetic fields, $\beta=100$, $\beta=10$, and $\beta=1$ are included for timesteps of two tenths of an orbit over the interesting three orbital period in which cooling causes thermal instabilities to develop and structure to evolve. Contours of the magnetic potential are plotted whenever the magnetic field is initialized.

The simple hydro case has the typical $\varepsilon=0.035$ (see Fig 11). As cooling is turned on, thermal instabilities rapidly form dense clouds. These clouds are shed off the central shock in the form of large parallel density perturbations, and flow downstream away from the arm. They are not all shed at exactly the same time intervals. These dense filaments maintain their continuity until almost a full orbit later, when the boundary periodicity brings them into contact with the arm. The filaments fragment and blend into the arm in this collision. As a result, the next set of filaments to leave the bar do not have the same perfectly parallel symmetry to the arm as the first set did. The arm is still fairly clear after the three orbits have ended, and the gas is distributed in the arm and in long density conglomerations which seem to start perpendicular to the central potential but are sheared out.

The low magnetic field case of $\beta=100$ (Fig 12) shows much the same initial response to the cooling function as did the previous case. Linear density filaments leave the central arm and re-collide after about one orbit, where the arm develops some transient spur-like substructures. However this structure soon gives way to large cloudlets interacting with the upstream arm front. There are no obvious differences between the final state of the cloudlets in this slightly magnetized

case with those of the unmagnetized case.

As β increases to 10 (Fig 13), the parallel filaments develop the tendency to fragment into small over-dense regions aligned along the magnetic field lines. This is because the magnetic pressure forces resist compression perpendicular to field lines, so the thermal instability can most easily develop with velocities in the azimuthal (field-aligned) direction. On the trailing edge of the arm, these small cloudlets are sheared out and form long spurs off the central spiral arm. These spurs persist for a little over half an orbit before they fragment into small and large clouds for the remaining orbits.

Finally, the strong field case with $\beta=1$ (Fig 14) shows clear suppression of the sharp density filaments characteristic of the unmagnetized or weakly magnetized cases. Instead of parallel fronts moving off the main shock and then fragmenting, the initial shock stays fairly steady and spurs form as the cooled gas is sheared out of the magnetic field lines. As time progresses, long strands of dense regions appear to form and finally break up into individual clouds. This case seems to remain more ordered at the long time scale than the previous weakly magnetized simulations.

3.4. Shock Profiles

By holding ε constant, we study the effects of the simplified cooling function and its interaction with magnetic fields on the density profiles of spiral potentials. These profiles show the averaged $\hat{\gamma}$ (azimuthal) density over the box size of 1 kpc. The time evolution of the profile for 2D simulations with no magnetic field, $\beta=100$, $\beta=10$, and $\beta=1$ is shown in Figures 15, 16, 17, and 18, respectively. Two profiles are plotted in each; the dotted line is smoothing over 10pc, while the solid line is smoothing over a typical observational resolution of 150pc (comparable to the resolution in Fig 4). The boxcar function used to smooth the profiles leaves discontinuous artifacts on the edges, so these spikes should be ignored.

Overall, cooling appears to initially cause the central region of the arm to collapse to a highly dense region, while density perturbations slough off and flow downstream. As time progresses, these perturbations return through the periodic boundary to re-collide with the arm. It seems that after this initial re-collision, the overall profile seems to settle. The arm maintains a large average overdensity, but the inhomogeneous cloudy structure due to cooling smoothes out the leading edge of the shock to create a more symmetric profile.

The magnetic field strength suppresses the initial growth of the perturbations resultant from cooling. The unmagnetized case has the largest perturbations and central density peak, while increasingly magnetized cases reduce the compression from cooling. The magnetic fields in the $\beta=1$ model suppress the sharp perturbations entirely, resulting in a very smooth and broad profile.

Comparison to the high resolution cases yield very similar results. Figures 19, 20, 21, and 22 show a variety of time averaged profiles from the 1D simulations with the same initial conditions.

The profiles must be time averaged over some part of the orbit to enable comparison with the 2D profiles. The unmagnetized case very clearly has both the largest and the most density perturbations as a result of cooling. The strongest magnetic field model, $\beta=1$, looks essentially the same as the isothermal case in 1D because the thermal instability is suppressed. The other magnetized cases also seem to have sharper shock front faces than for the lower resolution 2D models.

3.5. Temperature Scales

Typical temperature scales for the warm and cold components of the atomic medium are between 5000 and 8000 K for the warm neutral medium and around 60 K for the cold atomic medium (McKee & Ostriker 1977). These temperatures correspond to the stable regions in the equilibrium cooling curve. Figure 23 shows a time evolution of the gas temperature for a selected simulation. All the models have the same general temperature scales, so only one case is shown as an example.

The gas temperature begins in an isothermal distribution near 2020 K with small deviations of ± 10 . After cooling is turned on, there is a transitional period that lasts approximately one orbit as the gas condenses and cools. After this orbit, the dense regions of the medium settle into cool regions with characteristic minimum temperatures of 60 - 70 K. These cool clouds are interspersed between diffuse, warm regions with maximum temperatures between 7000-9000 K. This is consistent with the stable temperatures of the CNM and WNM.

3.6. Cloud Widths

Regardless of whether the model considered contains strong magnetic fields or no magnetic fields at all, the late time morphology of the gas is dominated by irregular clouds and long filaments (please refer back to figures 11, 12, 13, and 14). The clouds share the same characteristic widths of $\sim 20\text{-}70$ pc, or $\sim 5\text{-}15$ grid zones in the 256x256 resolution simulations. This is the same order of magnitude as the standard atomic cloud size of ~ 10 pc. However, higher resolution 2D simulations still need to be performed to ensure that this result is independent of our resolution.

4. Summary

This study investigated effects of thermal evolution for shaping the density structure of spiral density waves in the ISM. Cooling and heating of HI gas tend to produce a two phase structure. For unmagnetized cases, thermal instability initially produces elongated filaments parallel to the shock front. Magnetic fields restrain the geometry in which thermal instability develops in the dense gas, and thereby cause structures such as sheared spurs to develop at early times. At late times,

structure in models of all field strengths is similar, and consists of irregular clouds and filaments which have their highest concentration in the arm.

We also examined the effects of heating and cooling on the azimuthally averaged surface density profile of the spiral arm. The substructures caused by the thermal instability have the effect of smoothing out the density profile, creating a final profile at late times which greatly resembles observed spiral arm density profiles. Strong magnetic fields suppress much of the density redistribution caused by the cooling of gas, and thus strongly magnetized profiles appear less smoothed.

However preliminary, these results show great promise towards illuminating the complex gas dynamics involved in spiral arm structure. With the addition of a cooling term, we have come close to recreating the smooth density profiles that are actually observed for spiral galaxies. In addition, we see several morphological characteristics, such as spur formation, which may play a role in the ISM of real galaxies.

Future work will implement the new detailed cooling function to simulate a cloudy medium without the approximations inherent in the cooling fit used here. Increased time and spatial resolution will enable us to follow individual clouds more closely to resolve some of the details of the cloud-arm interaction. Particularly, larger resolution simulations are needed to verify that the qualitative conclusions made within this paper, such as those of characteristic cloud widths, are not resolution dependent. More study is needed to understand how magnetic fields are restricting the effects of cooling. Future work will also include a turbulent forcing term to break up large clouds.

REFERENCES

- Balbus, Steven A. 1988, ApJ, 324, 60
Balbus, Steven A. 1988, ApJ, 328, 395
Balbus, Steven A., & Cowie, Lennox L. 1985, ApJ, 297, 61
Combes, F., & Gerin, M. 1985, A&A, 150, 327
Cox, D.P., & Smith, B.W. 1974, ApJ, 189, L105
Evans, C.R., & Hawley, J.P. 1988, ApJ, 332, 659
Field, G.B., Goldsmith D.W., & Habing, H.J. (1969), ApJ, 158, 173
Gittins, D.M., Clarke, C.J., & Bate, M.R. (2003) MNRAS, 340, 841
Gittins, D.M., & Clarke, C.J. (2003), MNRAS349, 909

- Hawley, J.P., & Stone, J. M. 1995, Comput. Phys. Commun., 89,127
- Kim, Woong-Tae, & Ostriker, Eve C 2001, ApJ, 559, 70
- Kim, Woong-Tae, & Ostriker, Eve C 2002, ApJ, 570, 132
- Lubow, Stephen H., Balbus, Steven A., & Cowie, Lennox L. 1986, ApJ, 309, 496
- McKee, C.F.,& Ostriker,J.P. 1977, ApJ, 218, 148
- Piontek, Robert A., & Ostriker, Eve C. 2004, ApJ, 601, 905
- Regan, Michael W., Vogel, Stuart N., & Teuben, Peter J. 1997, ApJ, 482, L183
- Regan, Michael W., Sheth, Kartik, & Vogel, Stuart N. 1999, ApJ, 526, 97
- Roberts, W.W. 1969, ApJ, 158, 123
- Roberts, W.W., & Yuan, C. 1970, ApJ, 161, 877
- Sánchez-Salcedo, F.J, Vázquez-Semadeni, E., & Gazol, A. (2002) ApJ, 577, 768
- Schwarz, M.P. 1981, ApJ, 247, 77
- Shetty, Rahul et. al. 2005
- Shu, F.H., Milione, V., & Roberts, W.W. (1973) ApJ, 183, 819
- Shu, Frank H. 1992, The Physics of Astrophysics Volume 2, Gas Dynamics (Mill Valley, CA:University Science Books)
- Spitzer,L.,Jr. 1978, Physical Processes in the Interstellar Medium (New York:Wiley)
- Stone, J.M., & Norman, M.L. 1992a, ApJS, 80, 753
- Stone, J.M., & Norman, M.L. 1992b, ApJS, 80, 791
- Wolfire, Mark G., McKee, Christopher F., Tielens, A.G.G.M., & Bakes, E.L.O. (1995) ApJ, 443, 152
- Wolfire, Mark G., McKee, Christopher F., Hollenback, David, & Tielens, A.G.G.M. (2003) ApJ, 587, 278
- Woodward, Paul R. (1974) ApJ, 195, 61

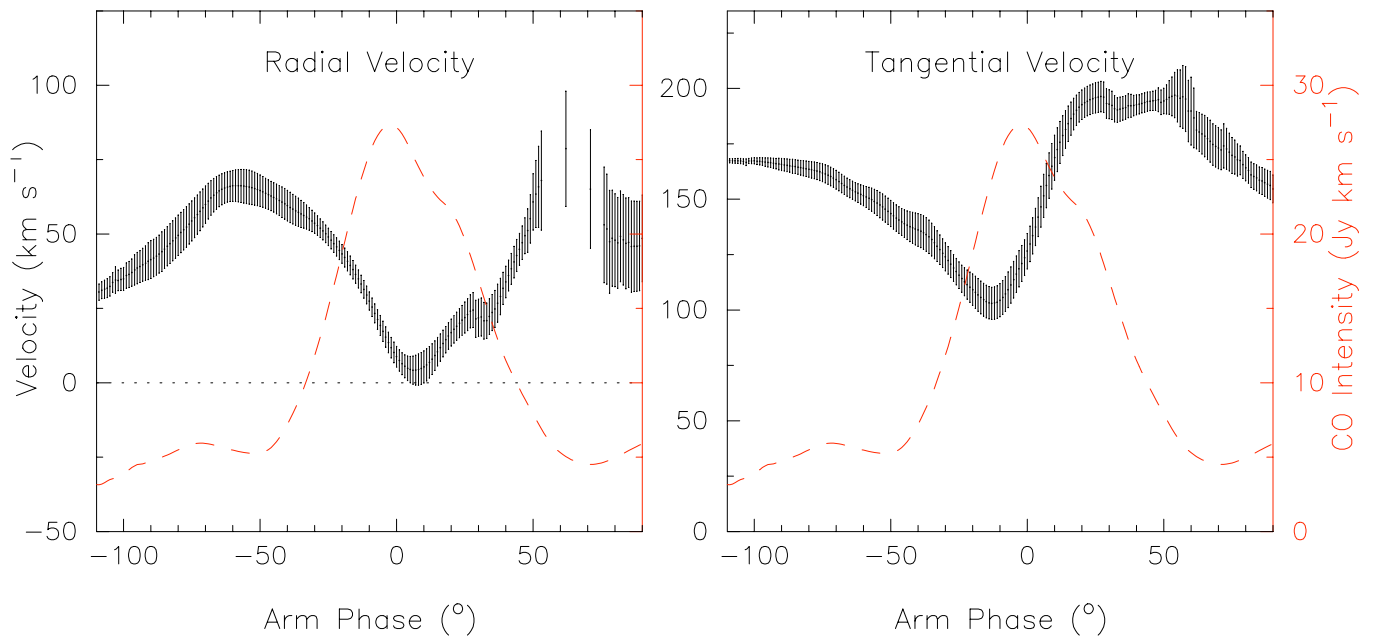


Fig. 1.— Radial and tangential velocity as a function of arm distance in a M51 arm segment, showing averaged CO intensity. Notice the smooth distribution of the shock profile which is unlike the sharp profiles produced in isothermal numerical simulations. Picture courtesy of Shetty et al. (2005).

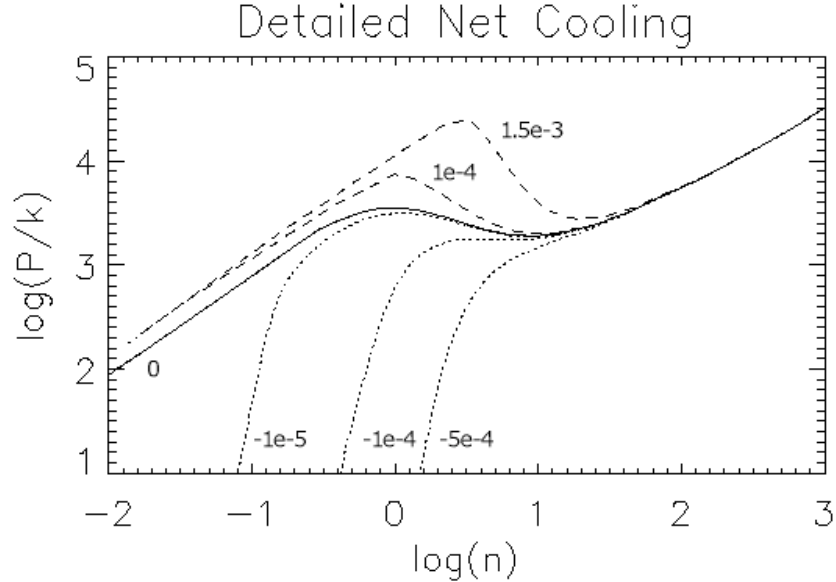


Fig. 2.— Contours of the detailed cooling function based directly on Wolfire et al. (1995, 2003). Values are of constant \mathcal{L} in units of $10^{22} \text{ergcm}^{-3}\text{sec}$. Net cooling occurs when $\mathcal{L} > 0$ and is indicated by dashed lines. Net heating occurs when $\mathcal{L} < 0$ (dotted lines). The solid line indicates the equilibrium curve.

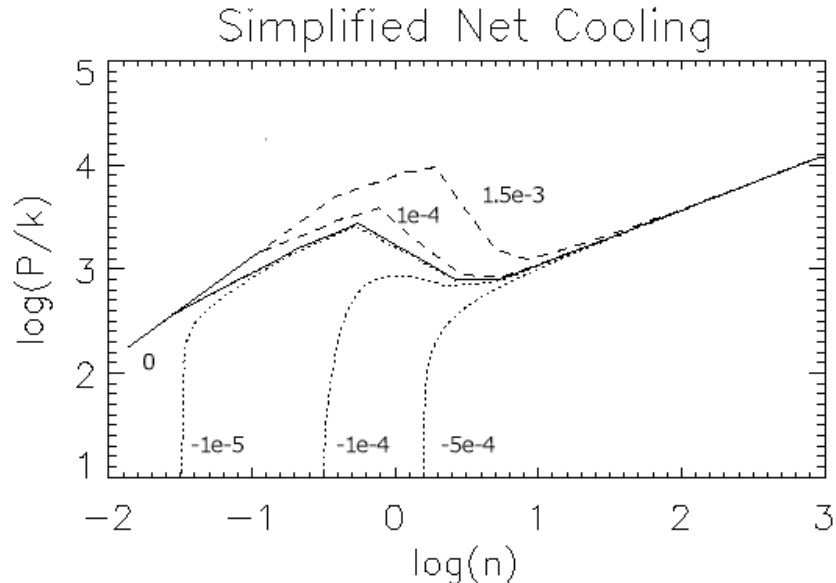


Fig. 3.— Contours of the simplified cooling function based on Sánchez-Salcedo et al. (2002). The same contours are plotted as specified above.

Table 1.

Dimensions	Time (orbits)	E_ϕ	β	Cooled or Isothermal
1D	7	0.02	*	iso
1D	7	0.03	*	iso
1D	7	0.035	*	iso
1D	7	0.04	*	iso
1D	7	0.05	*	iso
1D	7	0.03	*	cool
1D	7	0.035	*	cool
1D	7	0.04	*	cool
1D	7	0.05	*	cool
1D	7	0.035	100	cool
1D	7	0.03	10	cool
1D	7	0.035	10	cool
1D	7	0.04	10	cool
1D	7	0.05	10	cool
1D	7	0.03	2	cool
1D	7	0.035	2	cool
1D	7	0.04	2	cool
1D	7	0.05	2	cool
2D	6	0.035	*	iso
2D	6	0.035	*	cool
2D	6	0.035	100	cool
2D	6	0.035	10	cool
2D	6	0.035	1	cool

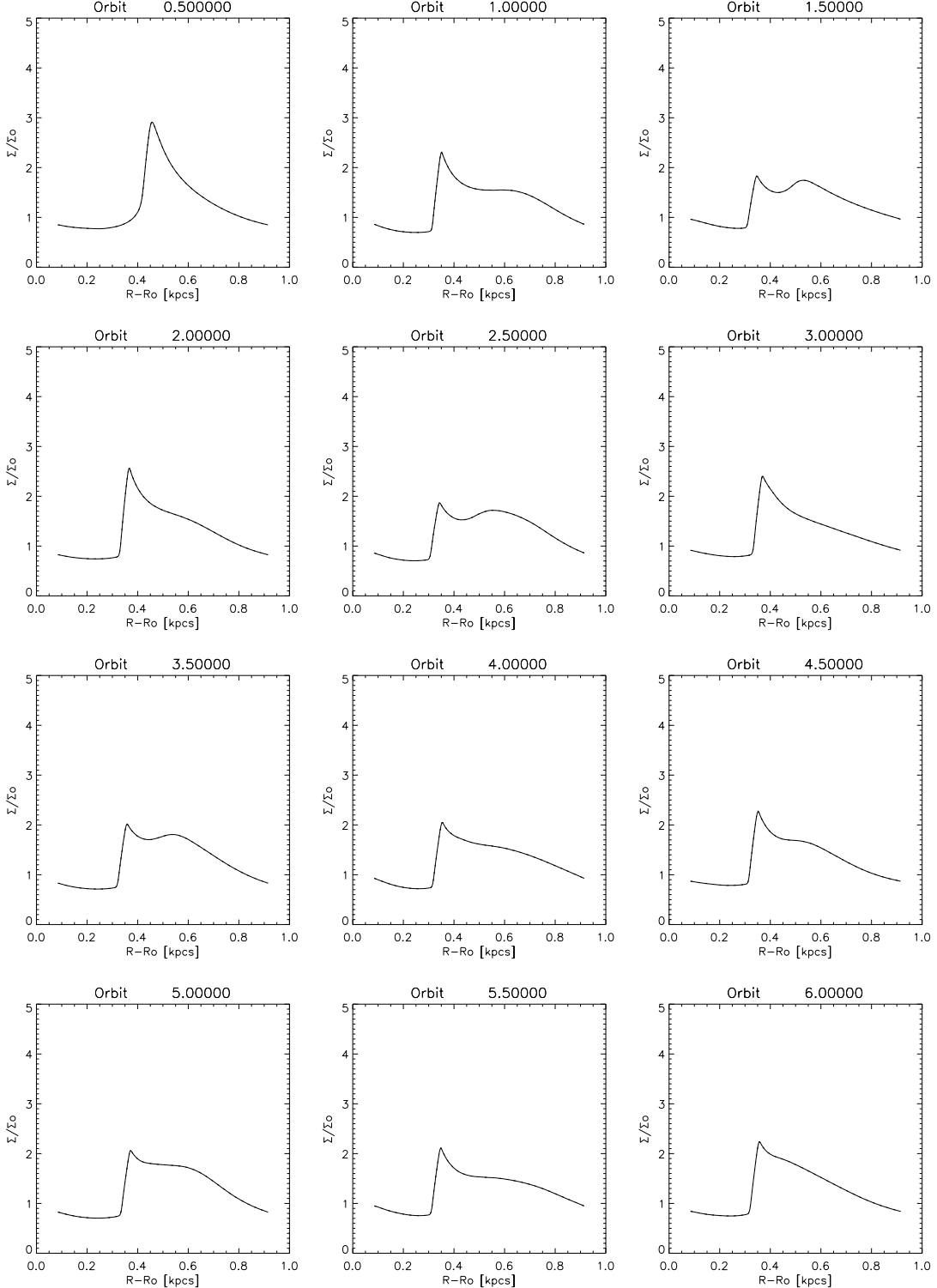


Fig. 4.— Results from an isothermal 2D simulation with $\varepsilon = 0.035$, showing the complex time evolution of the gas surface density profile of a spiral arm for 6 orbits. Profiles are averaged in the \hat{y} direction.

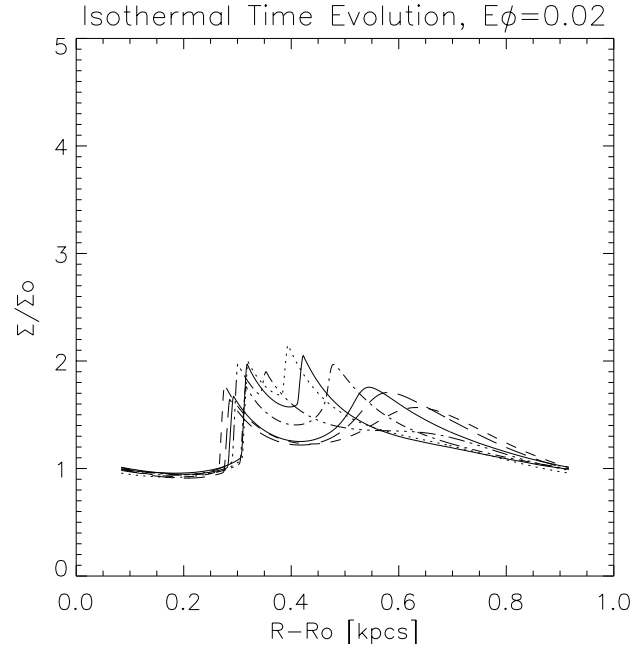


Fig. 5.— Results from an isothermal 1D simulation with $\varepsilon = 0.02$, showing the time evolution of the arm profile for orbits 3 through 6.

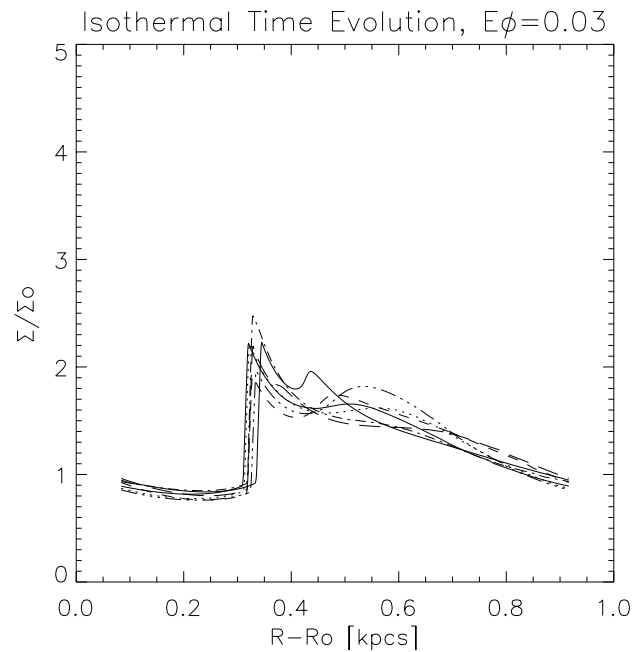


Fig. 6.— Results from an isothermal 1D simulation with $\varepsilon = 0.03$, showing the time evolution of the arm profile for orbits 3 through 6.

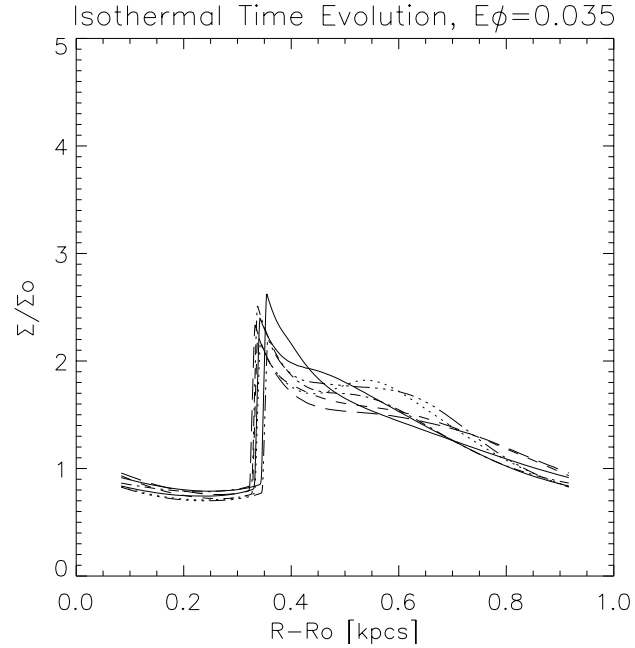


Fig. 7.— Results from an isothermal 1D simulation with $\varepsilon = 0.035$, showing the time evolution of the arm profile for orbits 3 through 6.

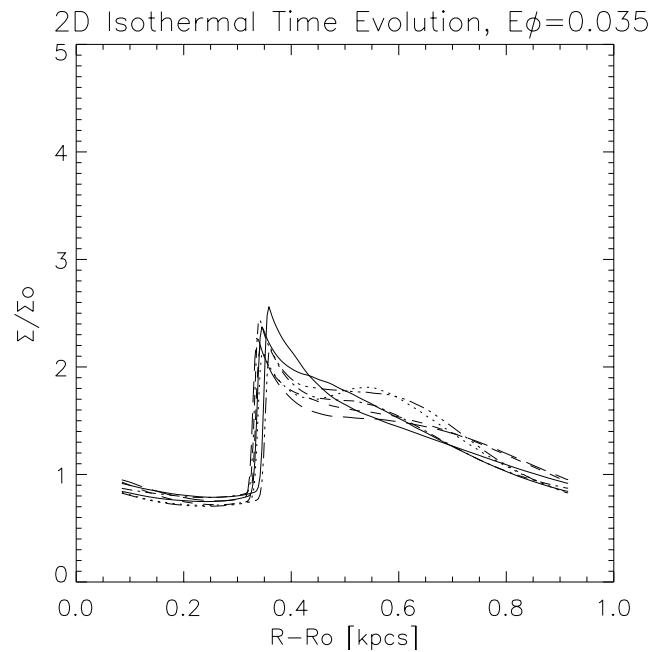


Fig. 8.— Results from an isothermal 2D simulation with $\varepsilon = 0.035$, showing the time evolution of the arm profile for orbits 3 through 6.

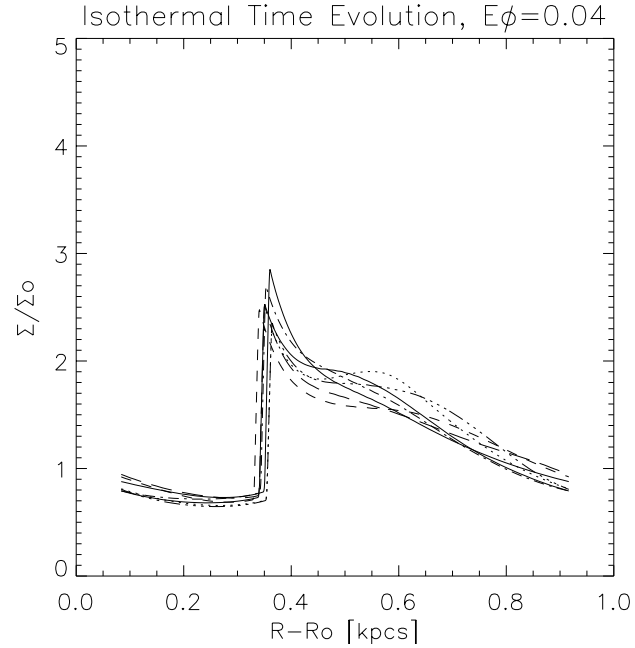


Fig. 9.— Results from an isothermal 1D simulation with $\varepsilon = 0.04$, showing the time evolution of the arm profile for orbits 3 through 6.

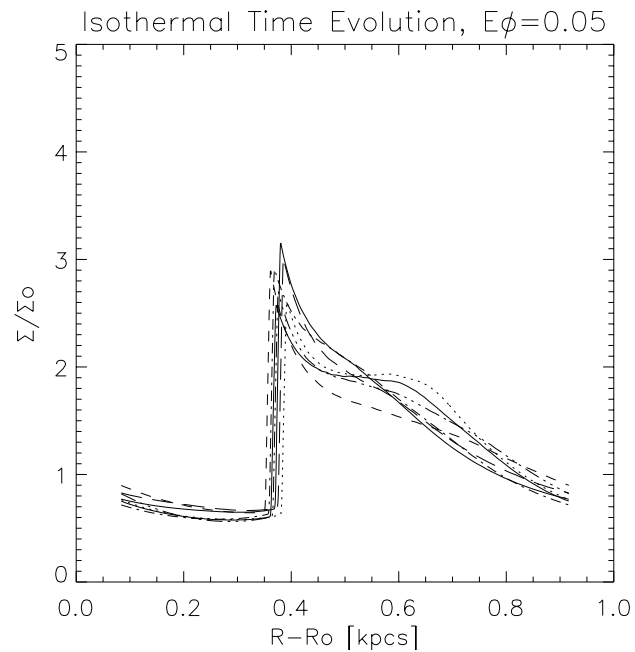


Fig. 10.— Results from an isothermal 1D simulation with $\varepsilon = 0.05$, showing the time evolution of the arm profile for orbits 3 through 6.

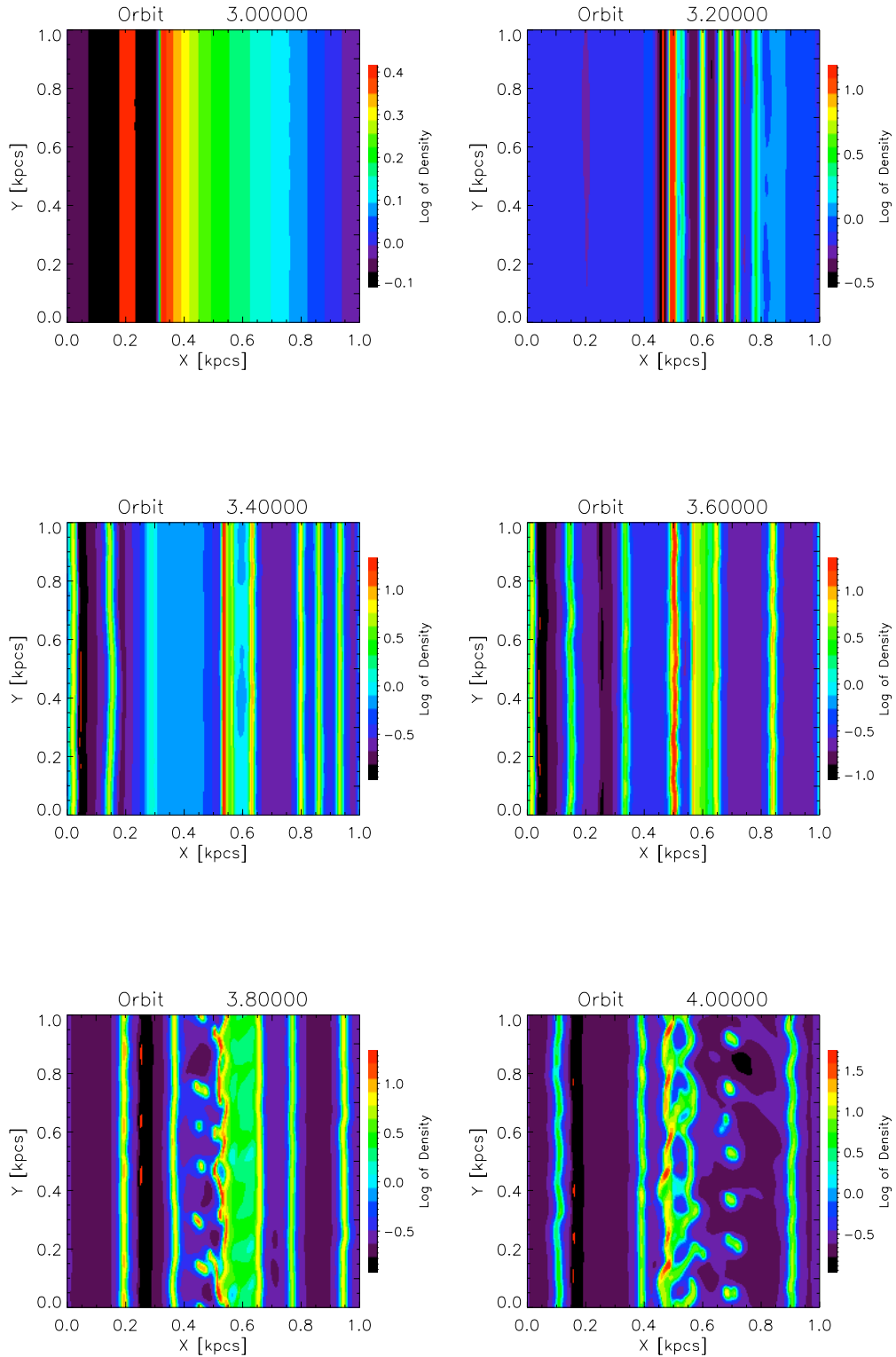


Fig. 11.— The detailed timescale evolution of a 2d model. This model has $\varepsilon = 0.035$ and no magnetic fields.

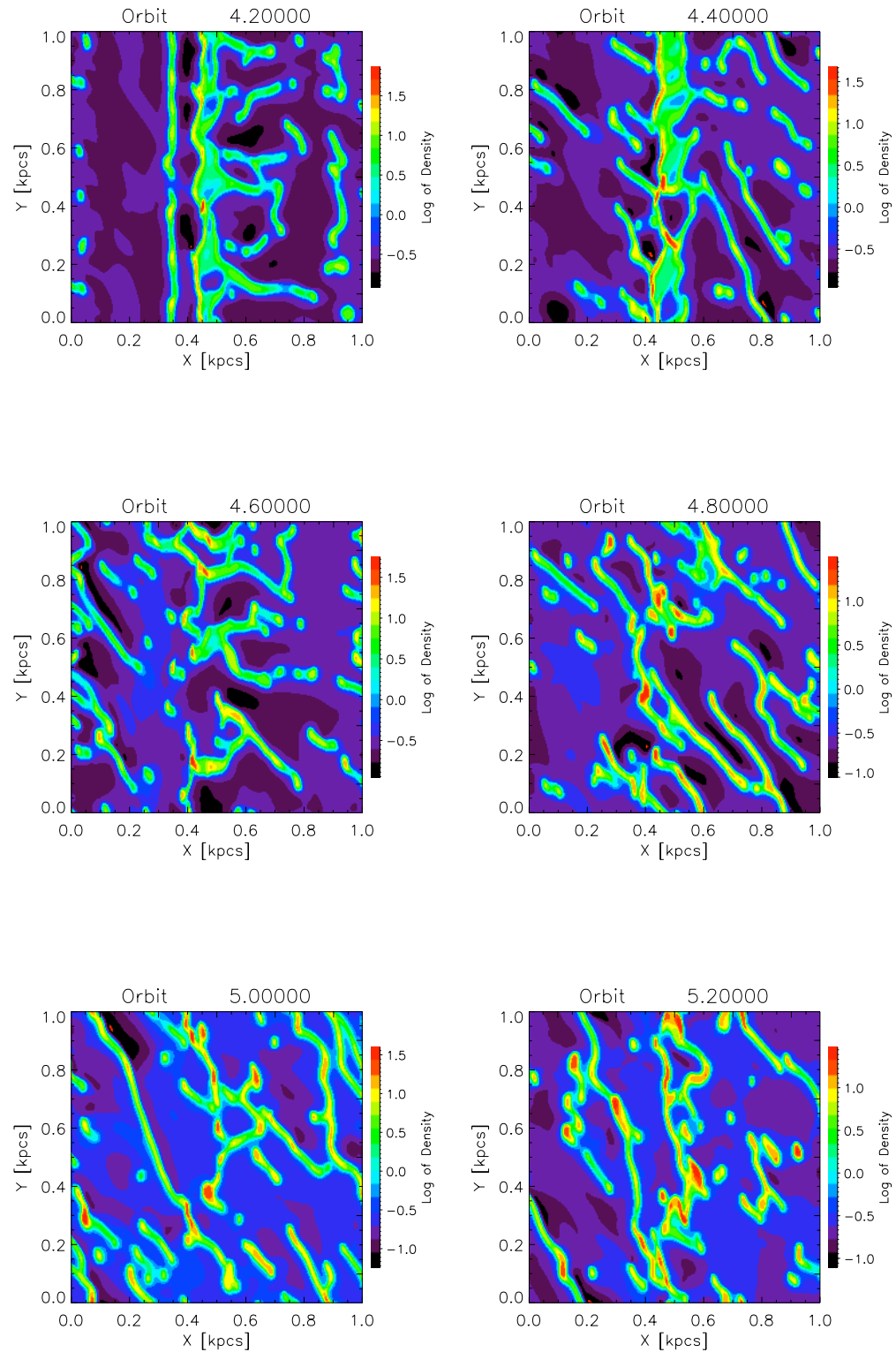


Fig. 11.— Continued from previous page.

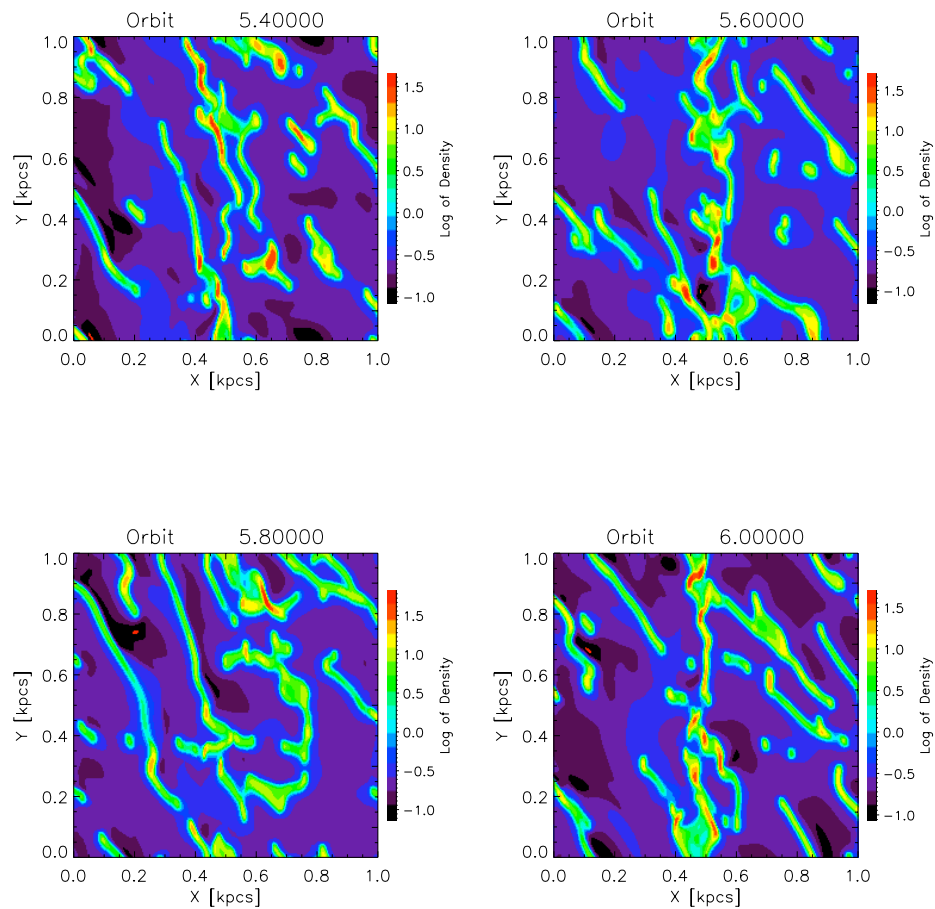


Fig. 11.— Continued from previous page.

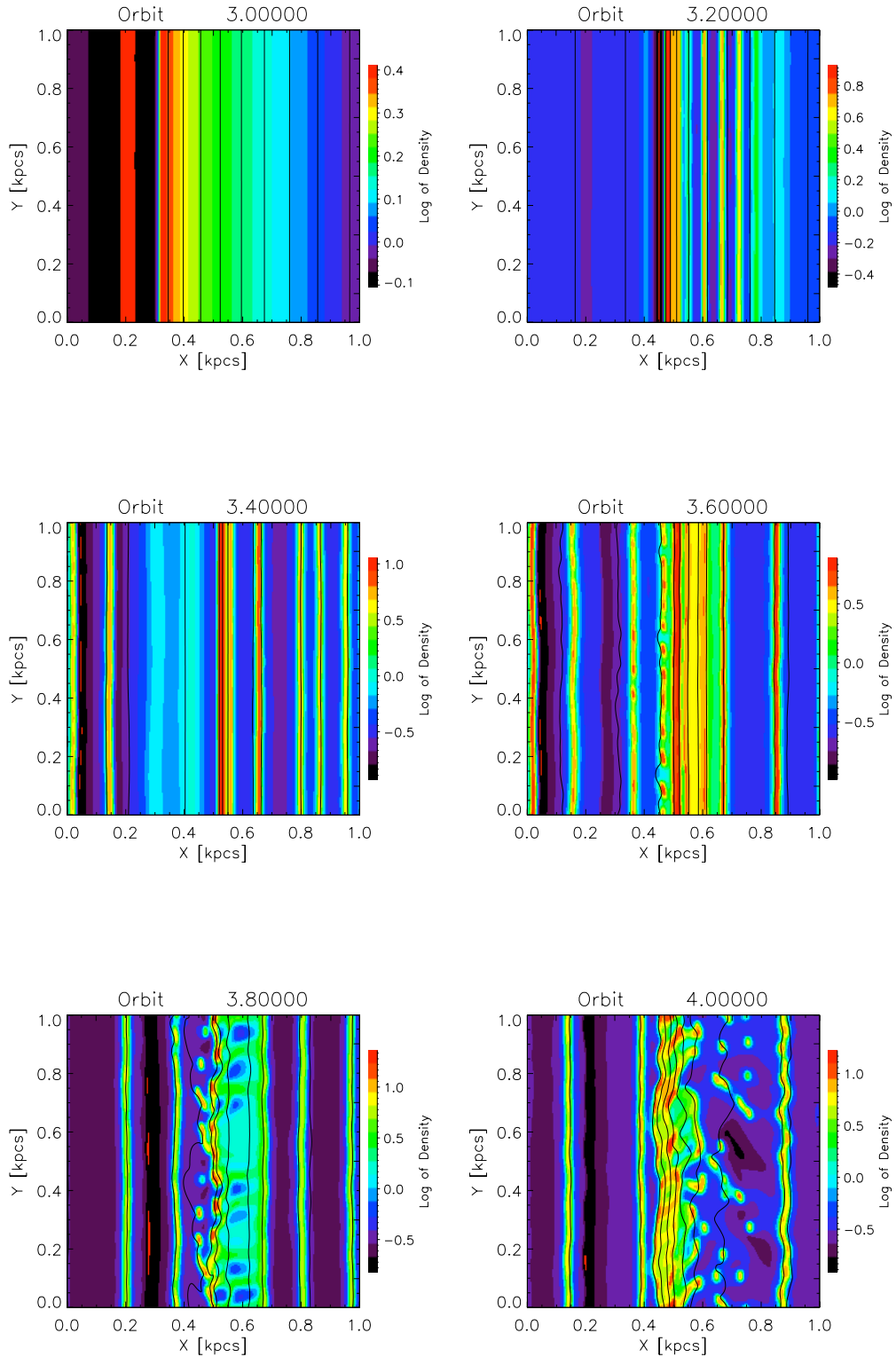


Fig. 12.— The detailed timescale evolution of a 2d model. This model has $\varepsilon = 0.035$ with $\beta=100$.

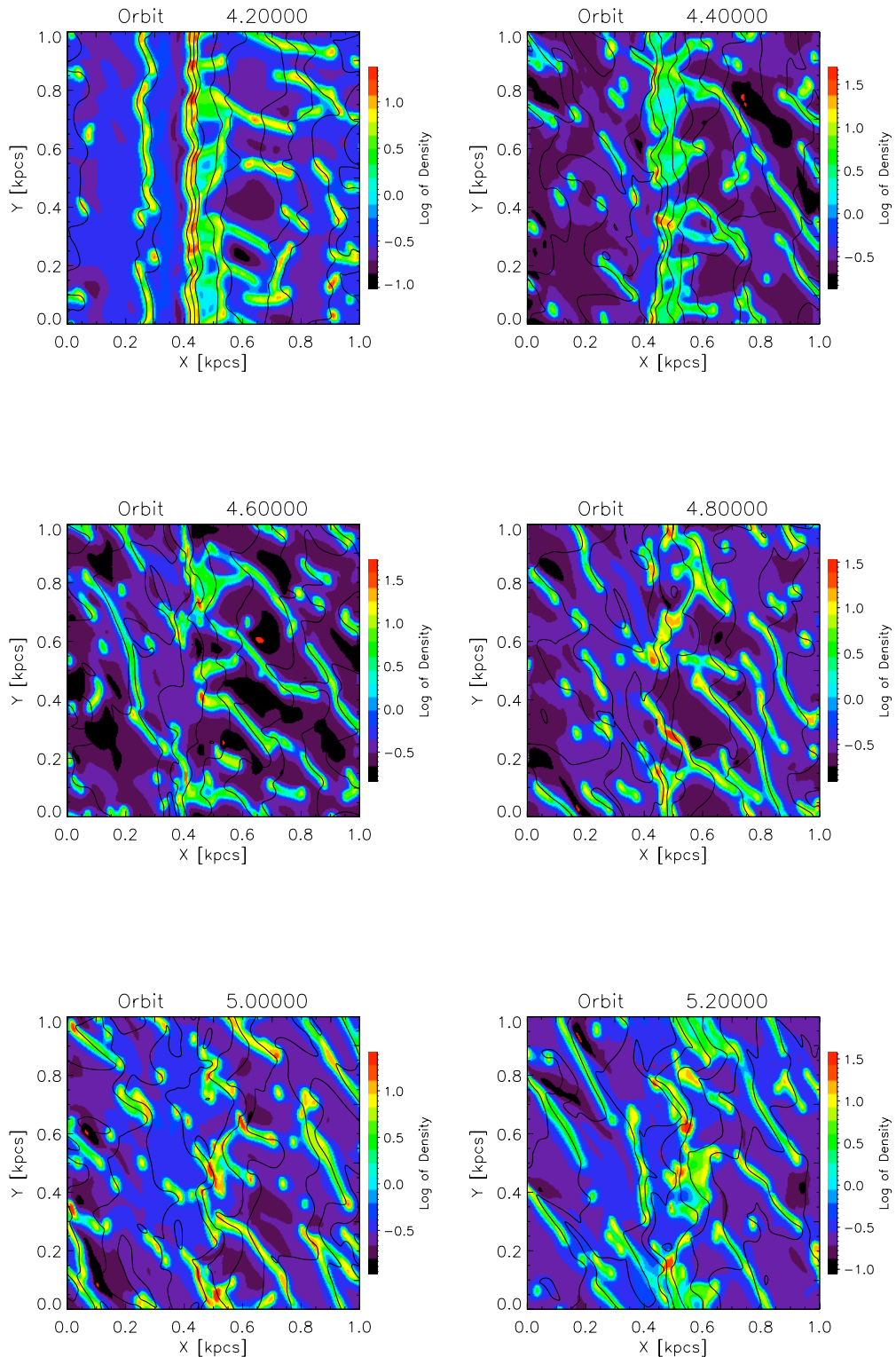


Fig. 12.— Continued from previous page.

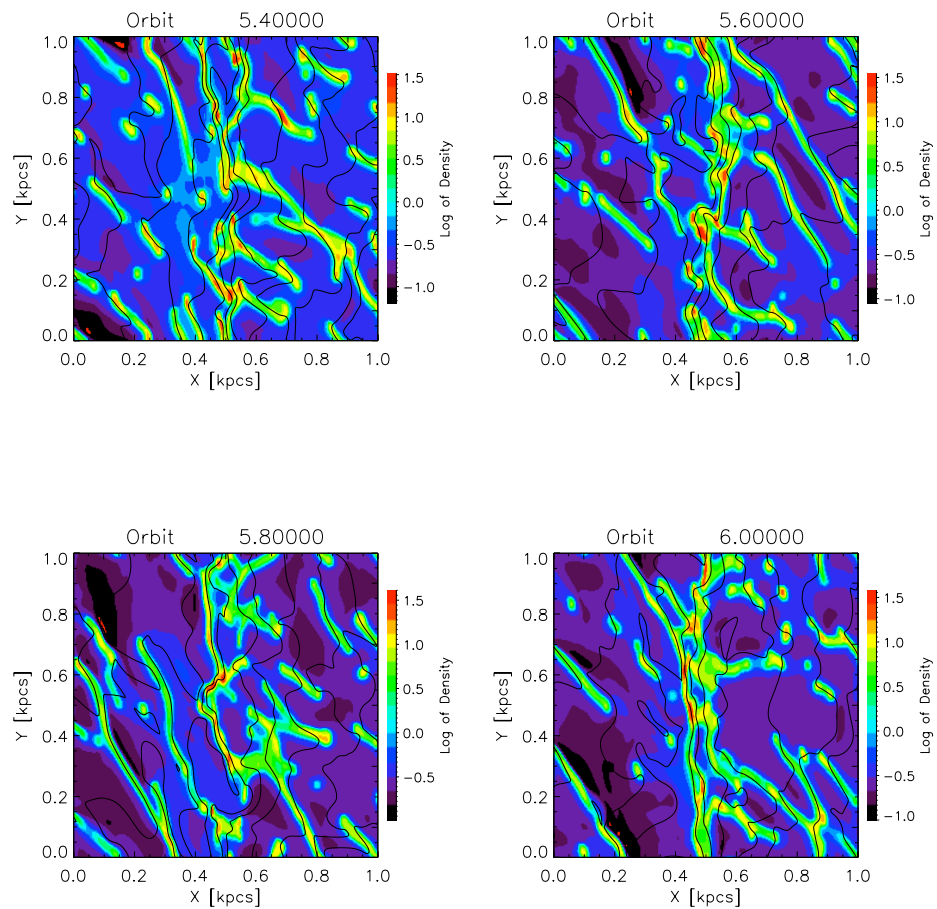


Fig. 12.— Continued from previous page.

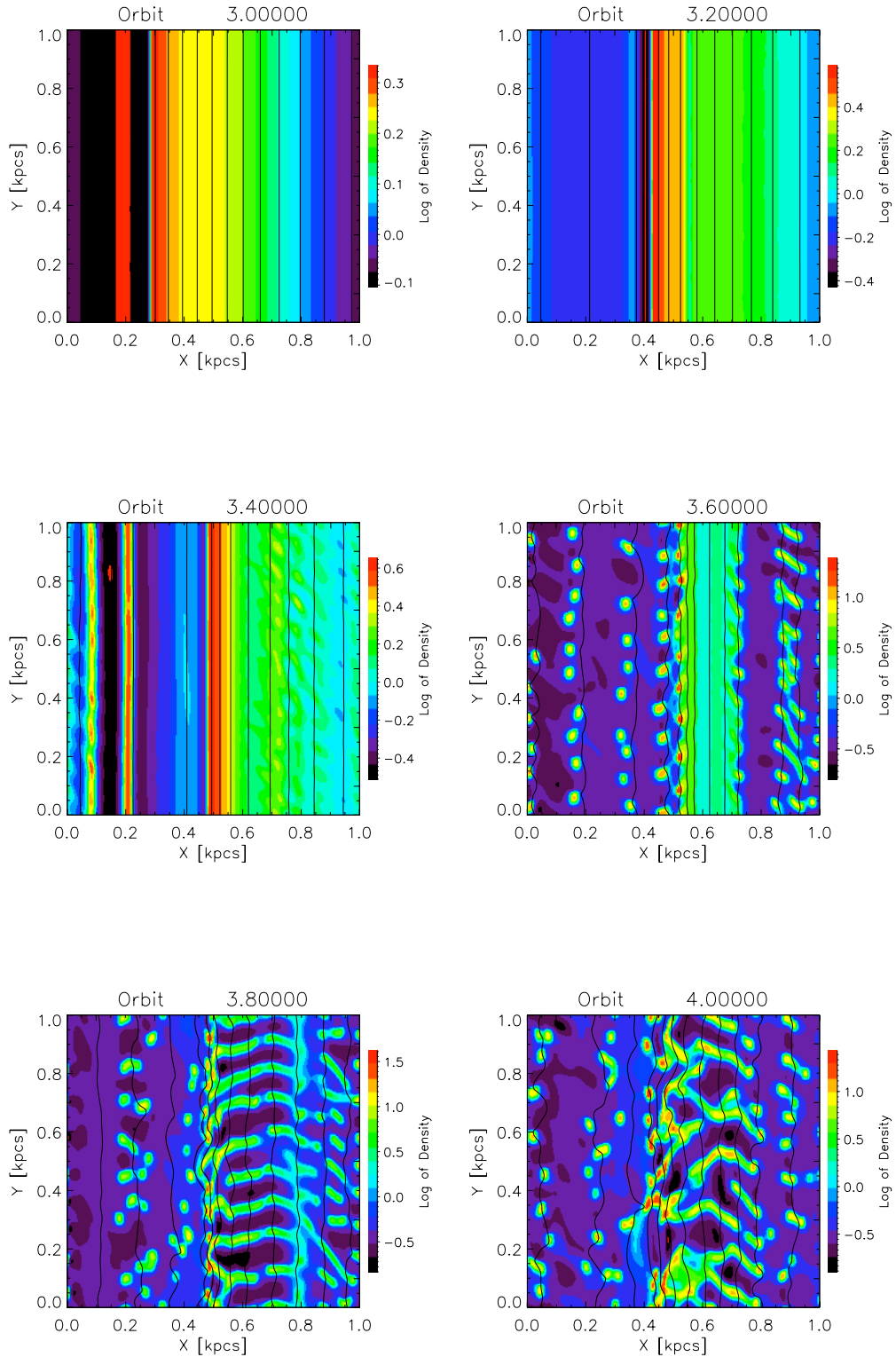


Fig. 13.— The detailed timescale evolution of a 2d model. This model has $\varepsilon = 0.035$ with $\beta=10$.

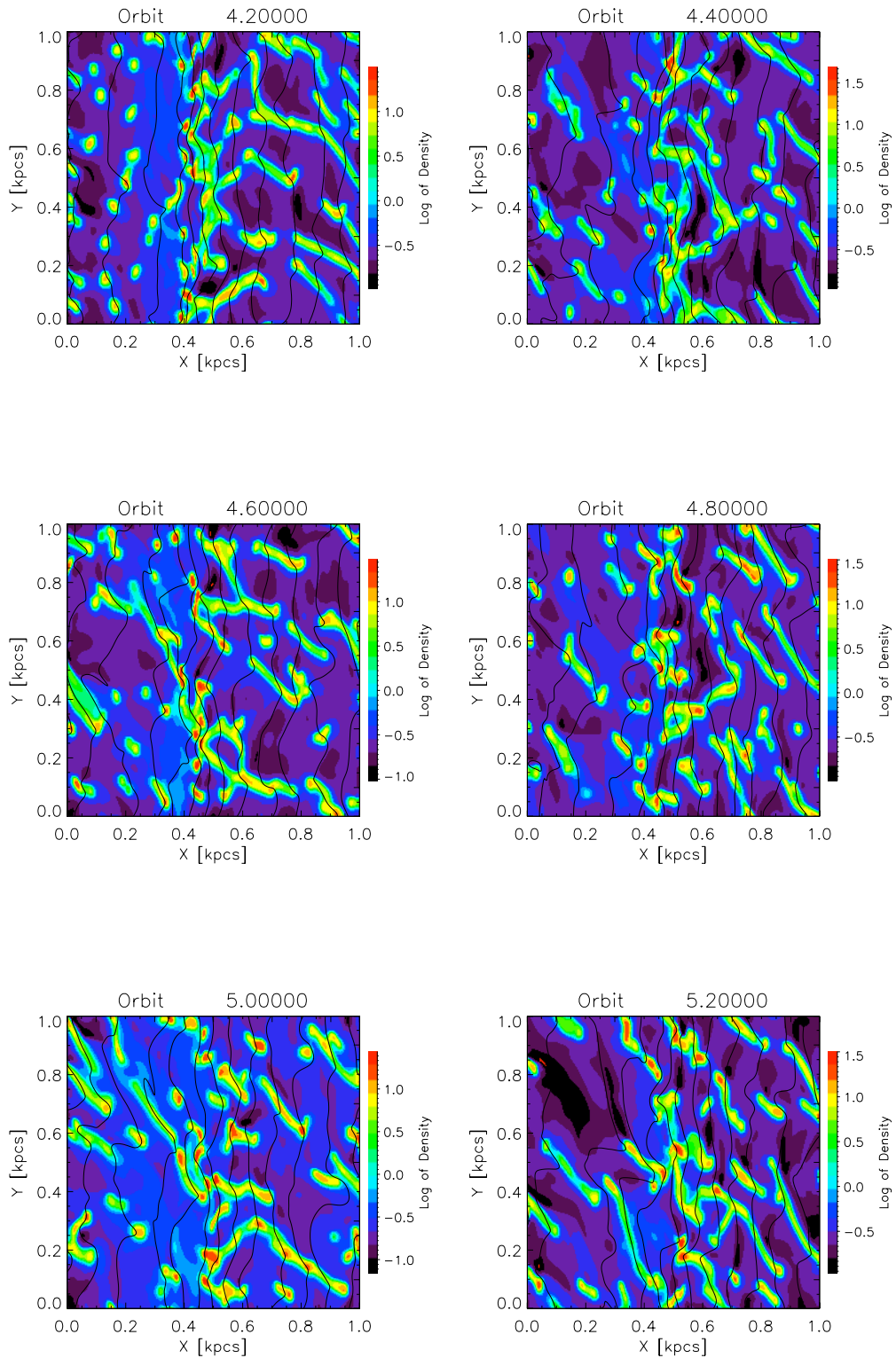


Fig. 13.— Continued from previous page.

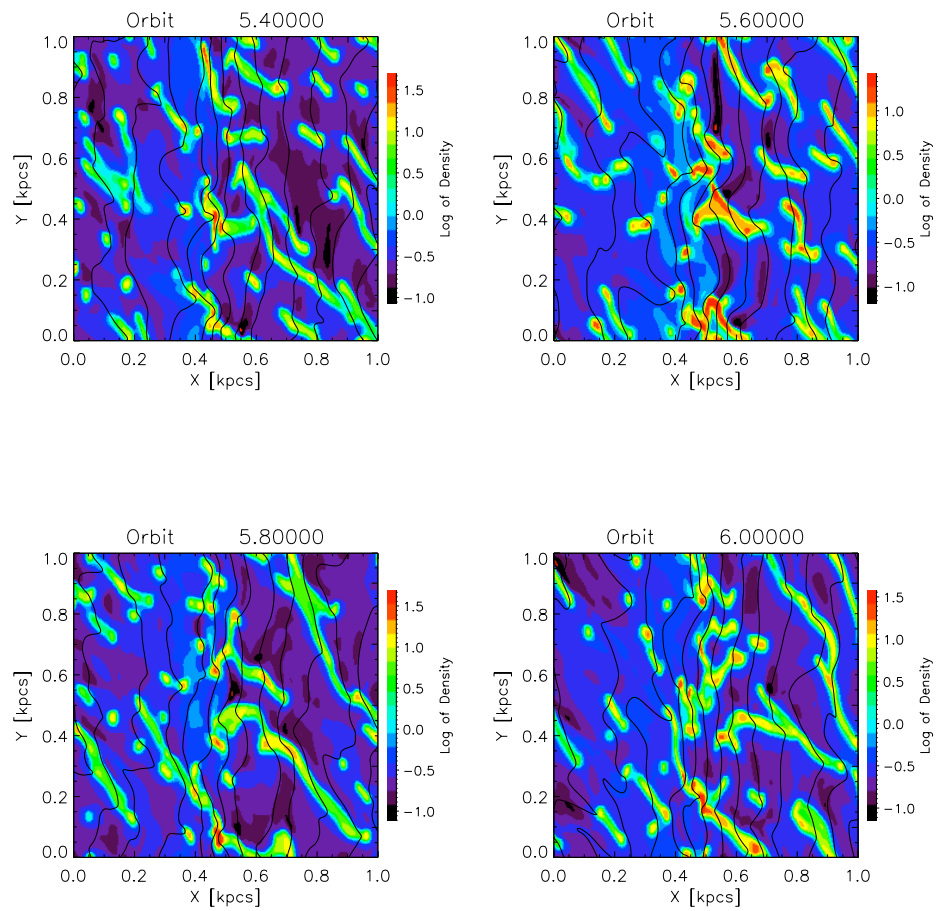


Fig. 13.— Continued from previous page.

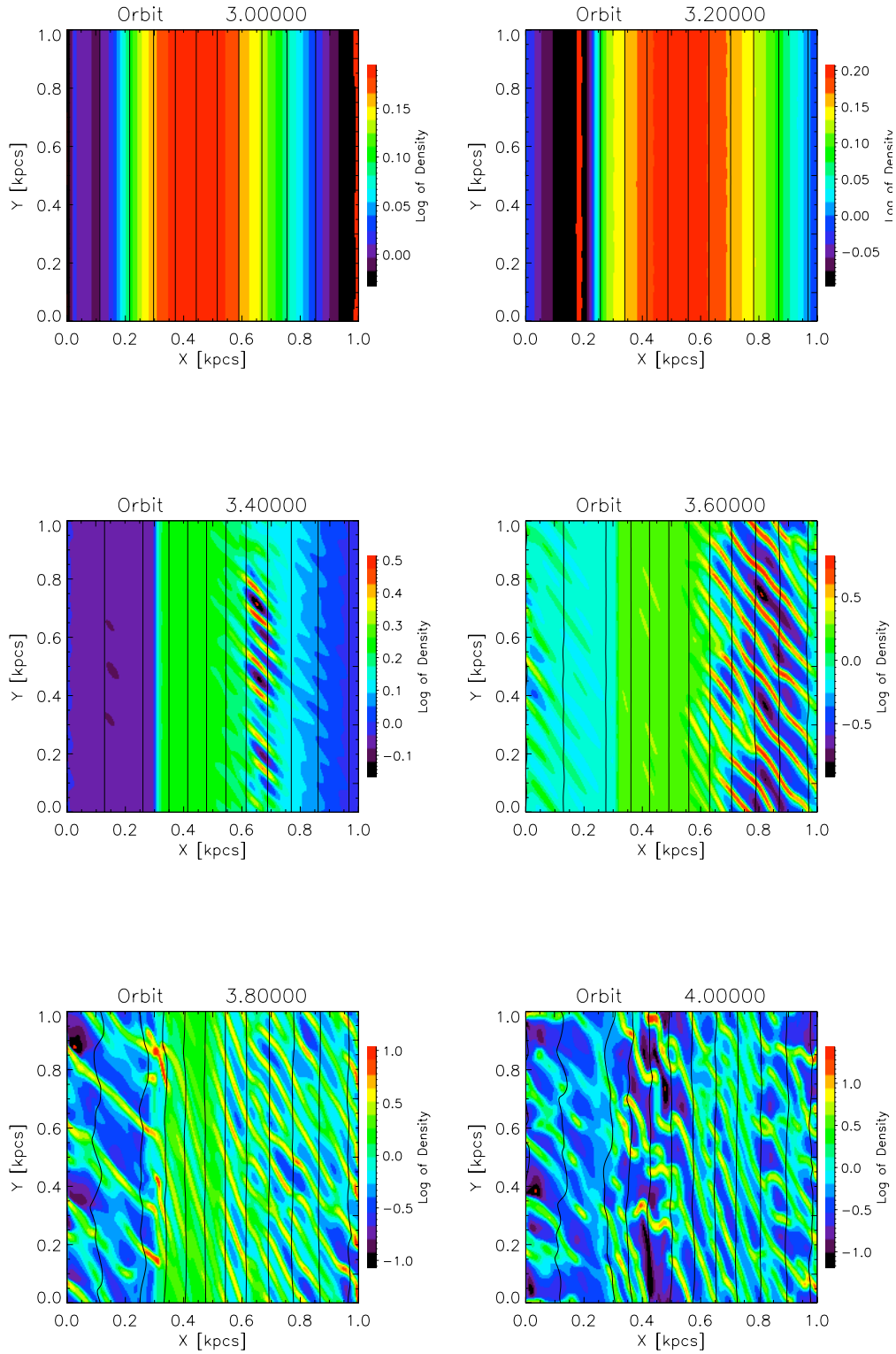


Fig. 14.— The detailed timescale evolution of a 2d model. This model has $\varepsilon = 0.035$ with $\beta=1$.

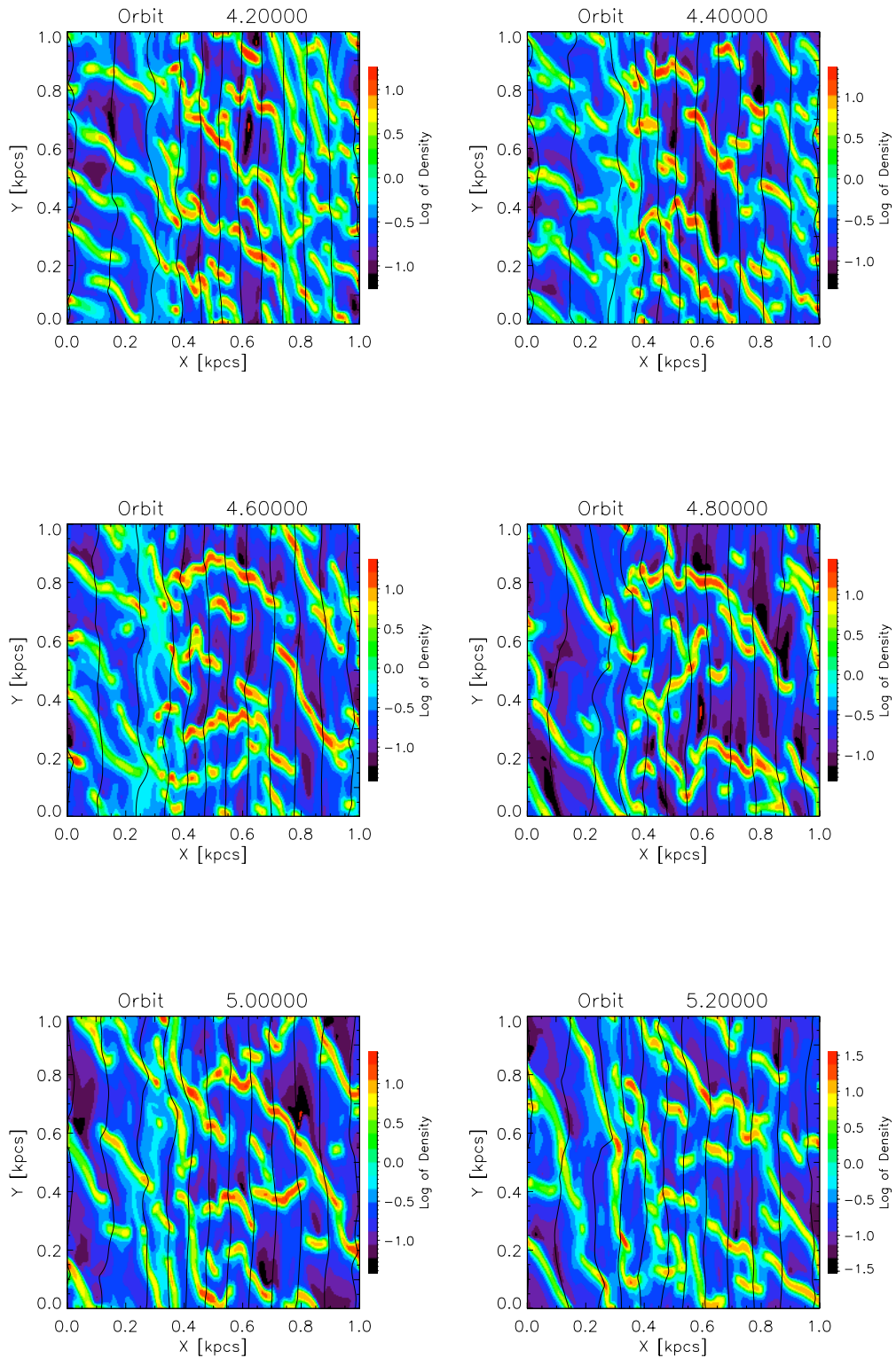


Fig. 14.— Continued from previous page.

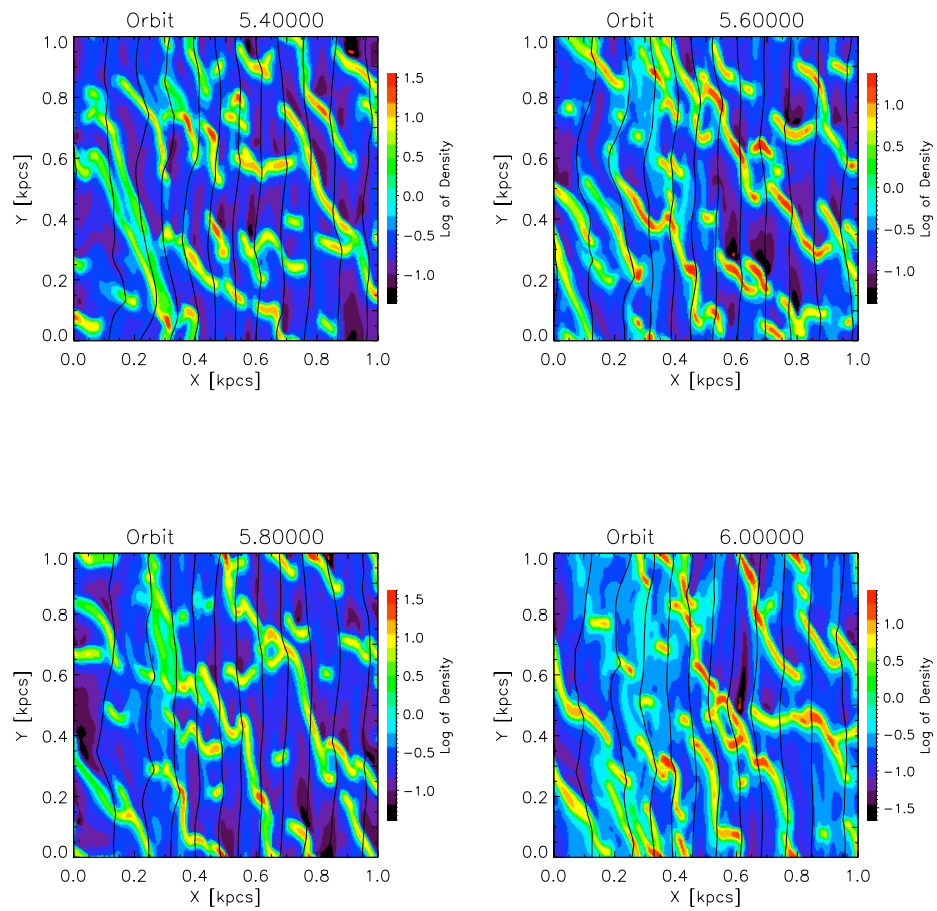


Fig. 14.— Continued from previous page.

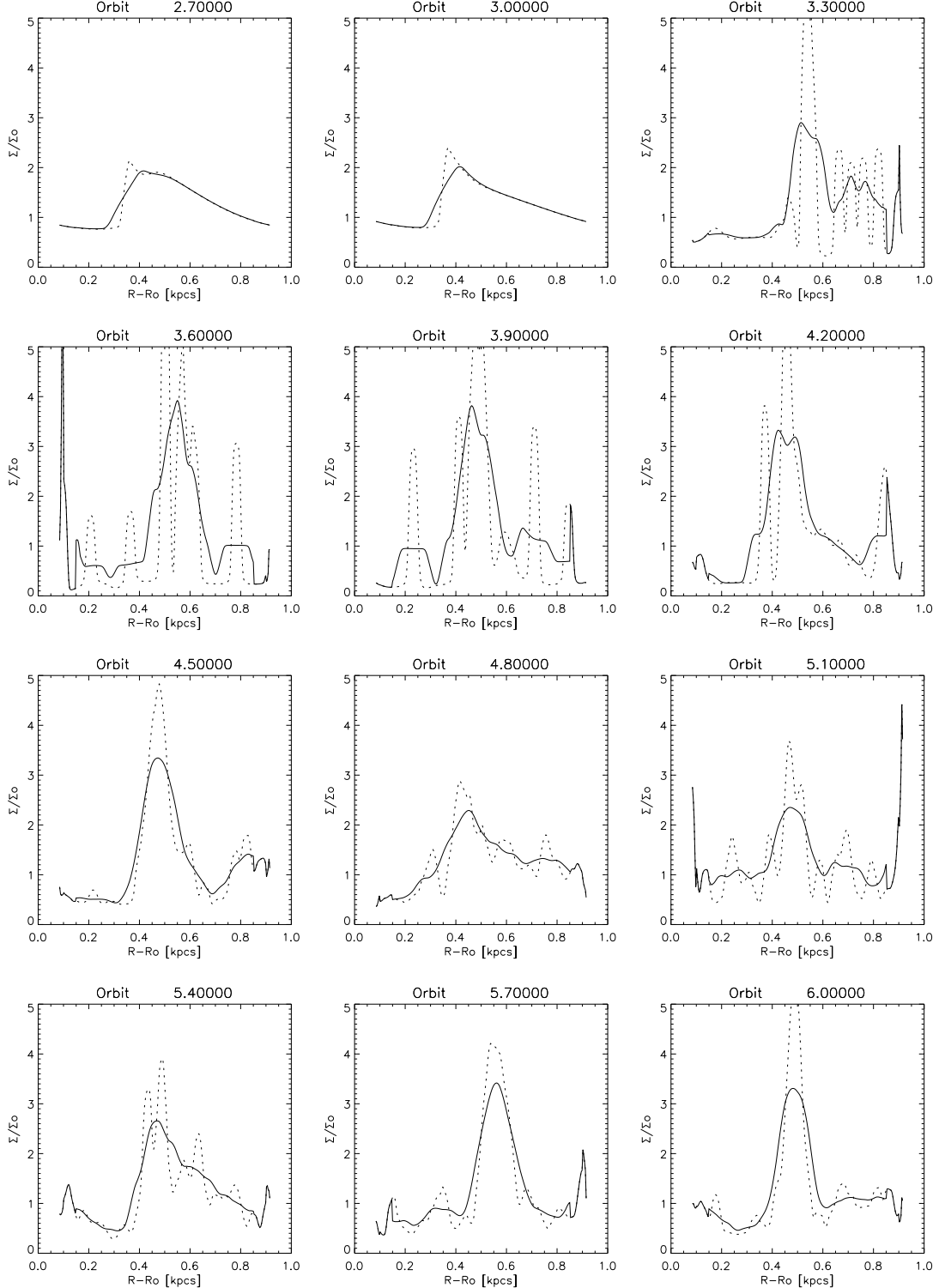


Fig. 15.— Results from a 2D simulation with $\varepsilon = 0.035$ with no magnetic fields, showing the time evolution of the cooled arm profile over the last three orbits. The solid line is smoothing over typical observational accuracies of 150 pc, while the dotted line is smoothing over 10 pc.

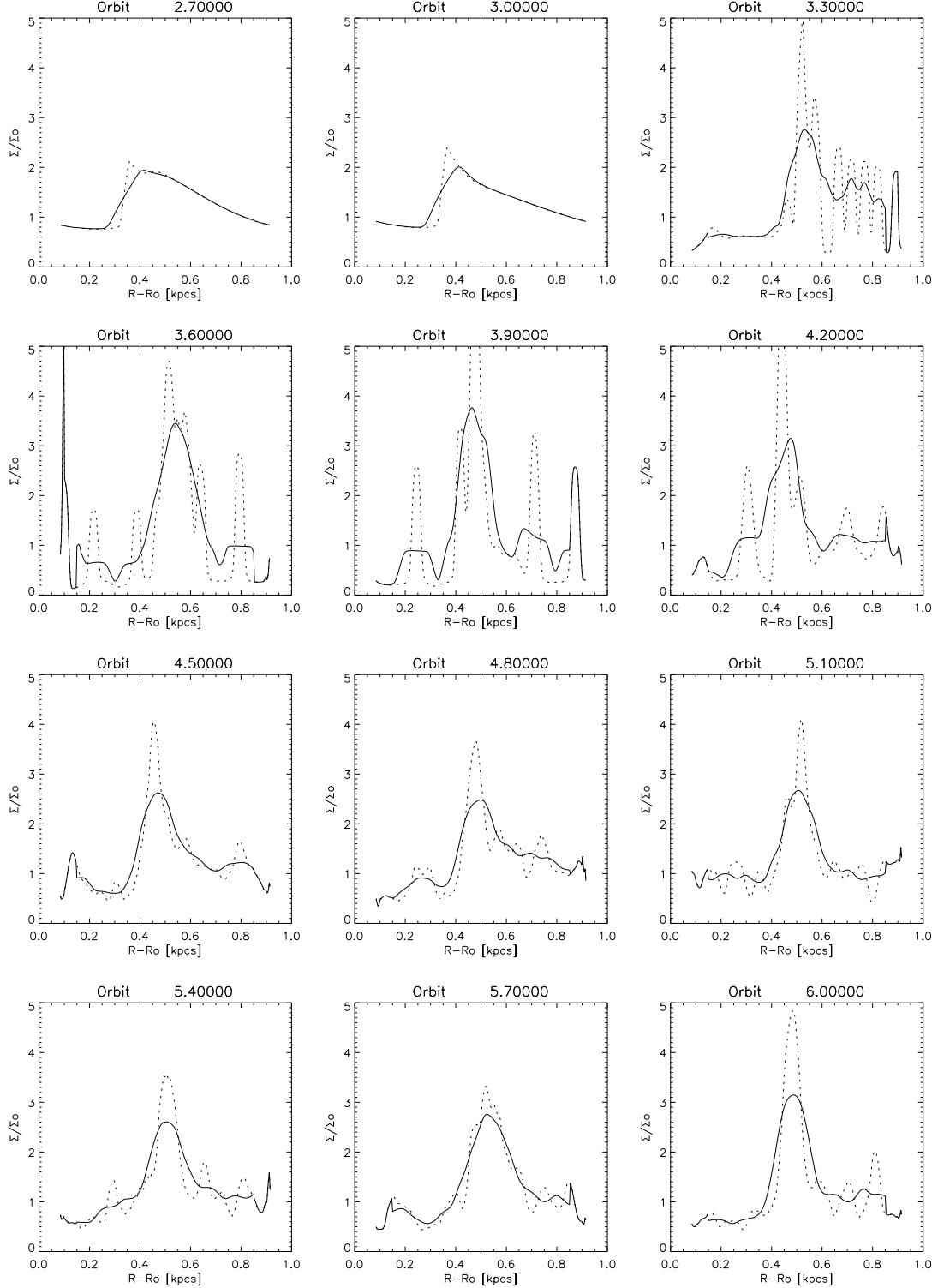


Fig. 16.— Same as Fig 15, but with $\varepsilon = 0.035$ and $\beta = 100$.

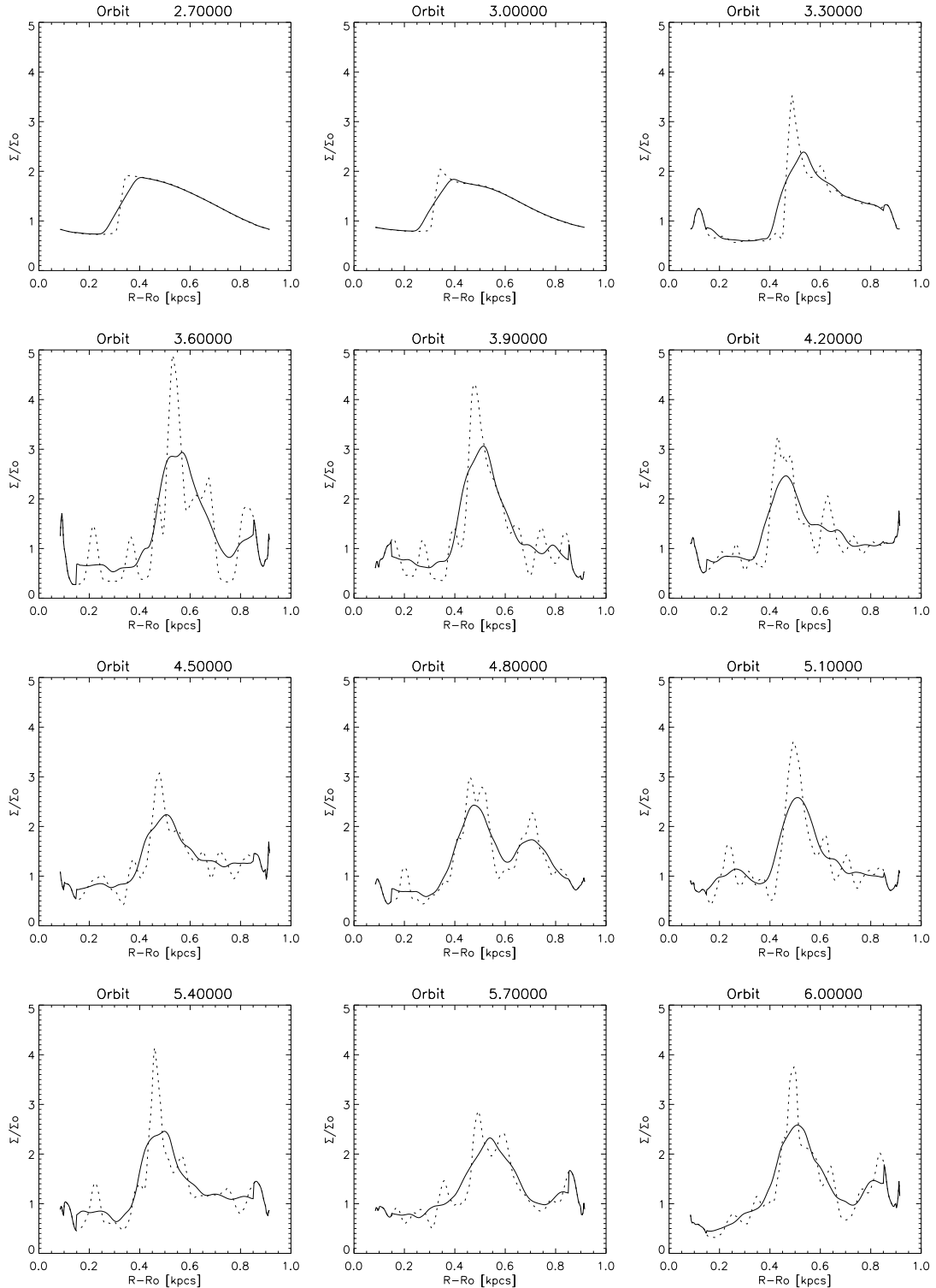


Fig. 17.— Same as Fig 15, but with $\varepsilon = 0.035$ and $\beta = 10$.

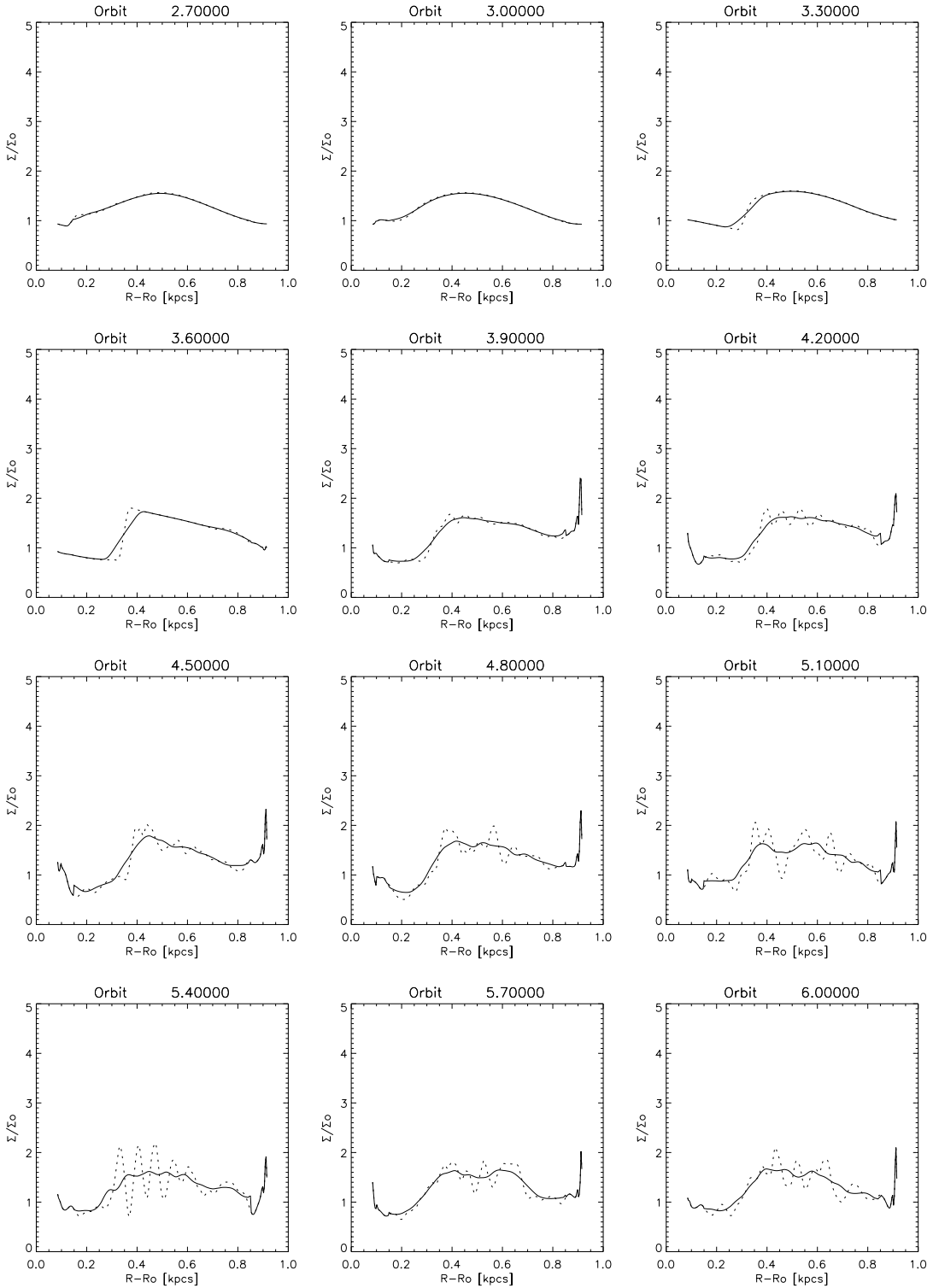


Fig. 18.— Same as Fig 15, but with $\varepsilon = 0.035$ and $\beta = 1$.

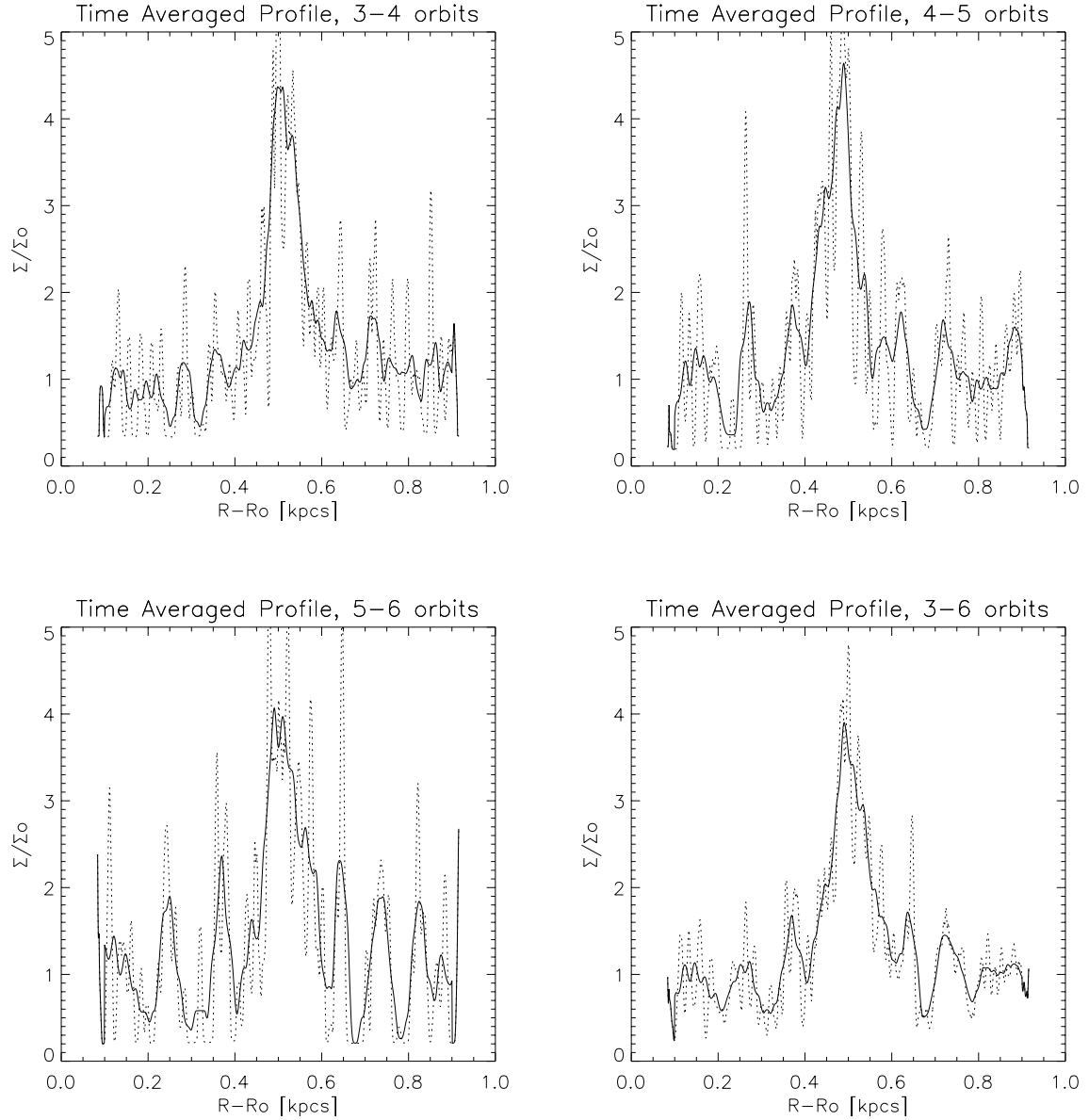


Fig. 19.— 1D time averaged profiles of $\varepsilon = 0.035$ with no magnetic fields. The solid line is smoothing over typical observational accuracies of 150 pc, while the dotted line is smoothing over 10 pc.

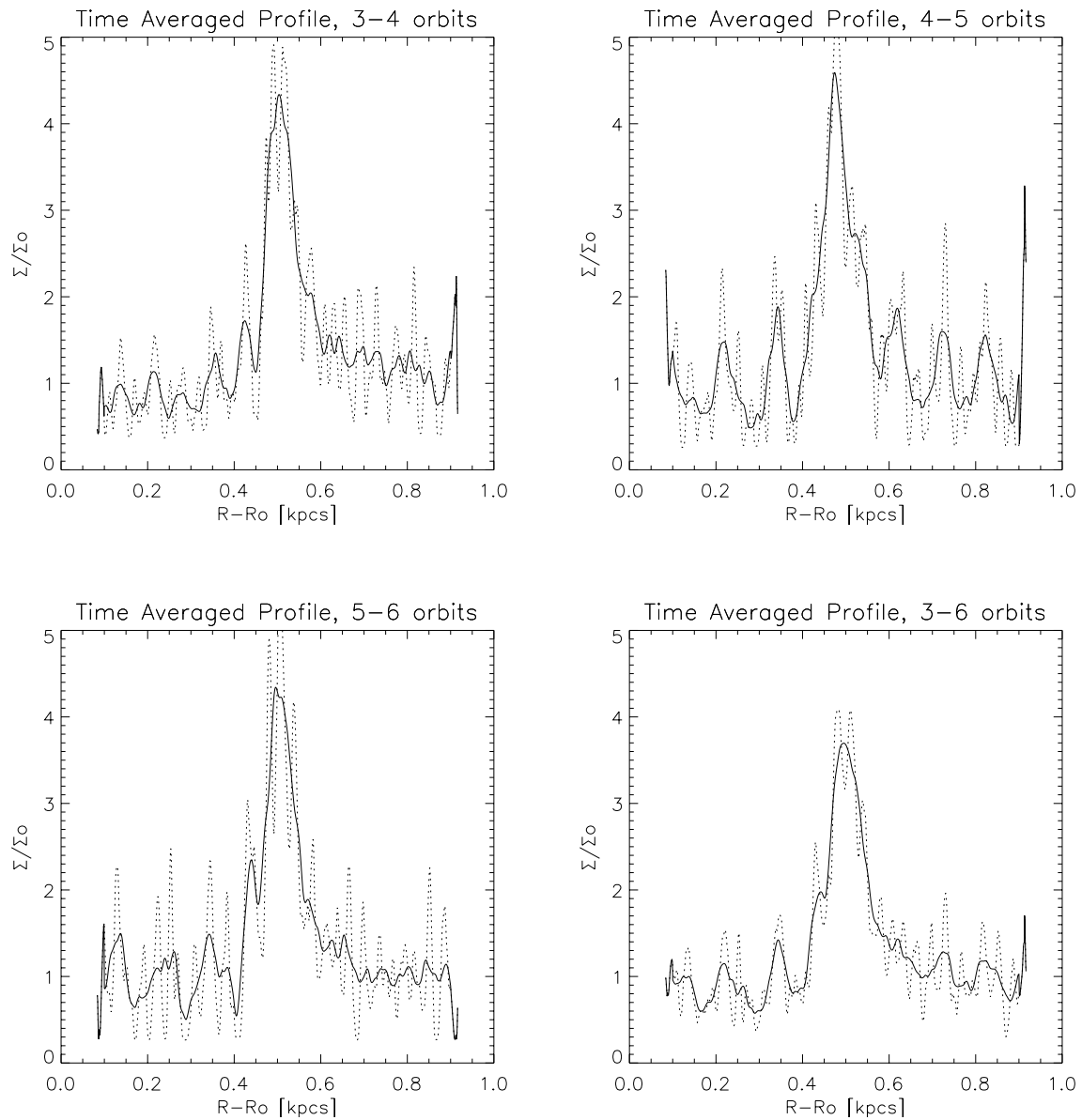


Fig. 20.— Same as Fig 19, but with $\varepsilon = 0.035$ with $\beta=100$.

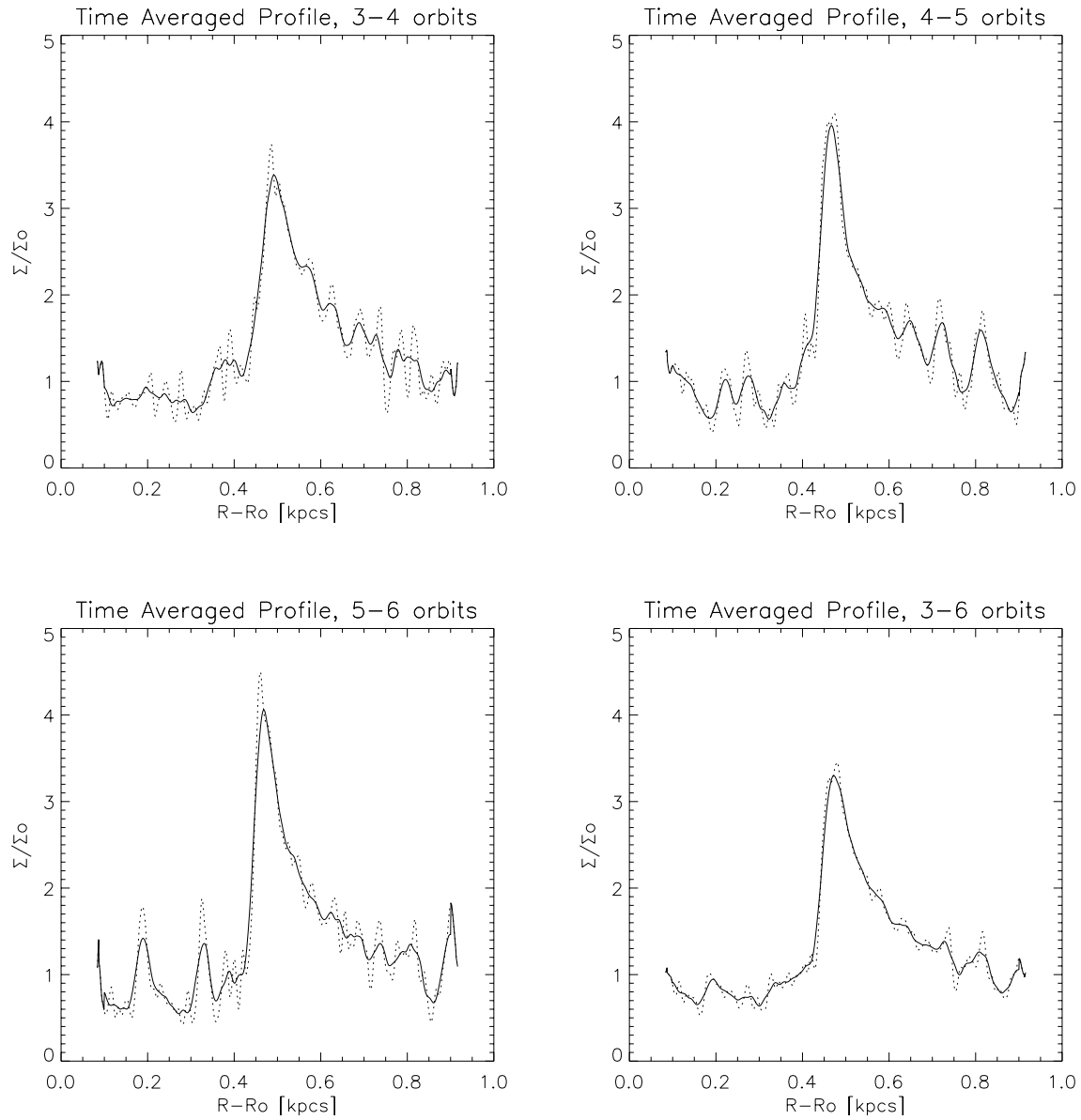


Fig. 21.— Same as Fig 19, but with $\varepsilon = 0.035$ with $\beta=10$.

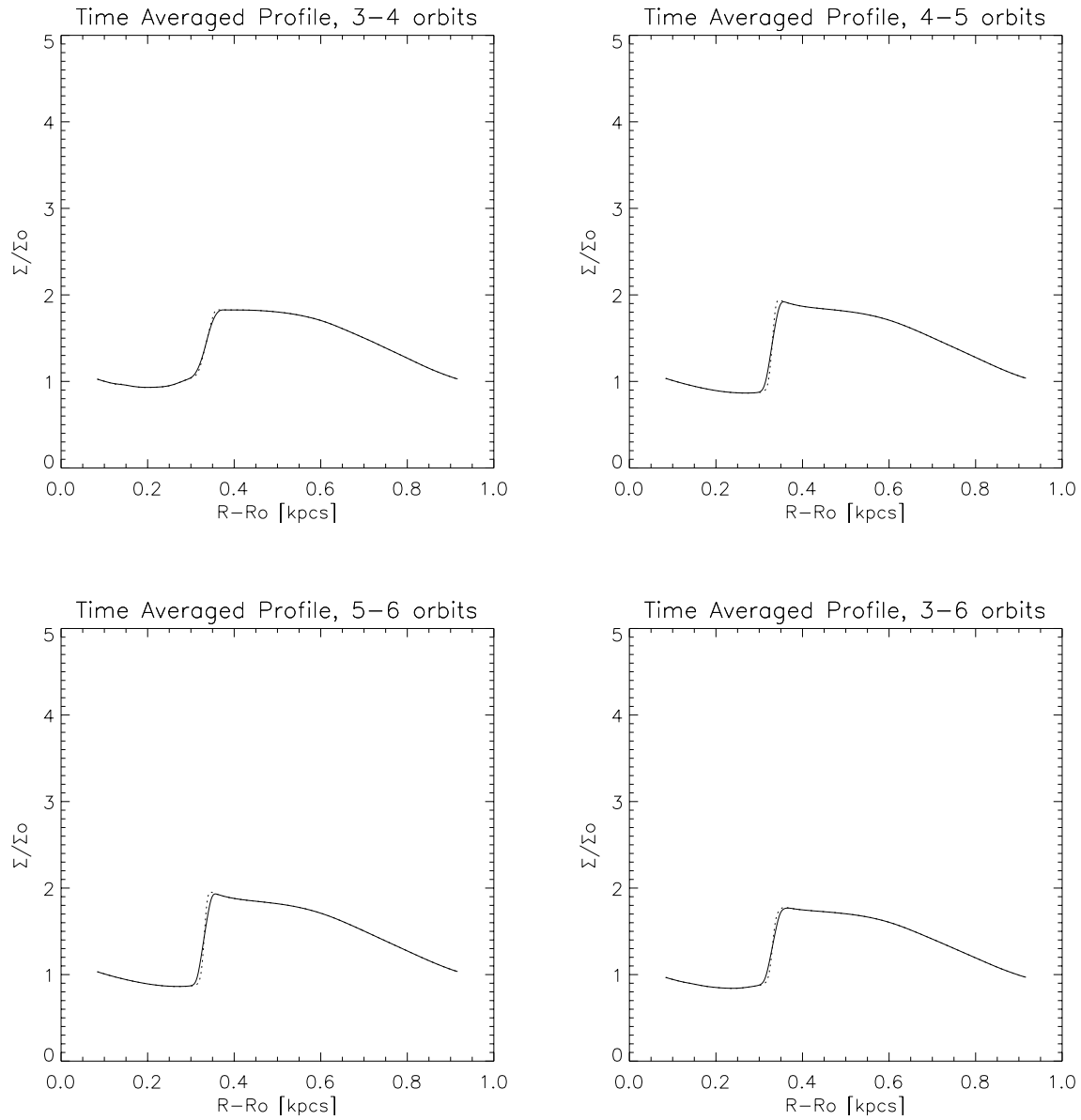


Fig. 22.— Same as Fig 19, but with $\varepsilon = 0.035$ with $\beta=1$.

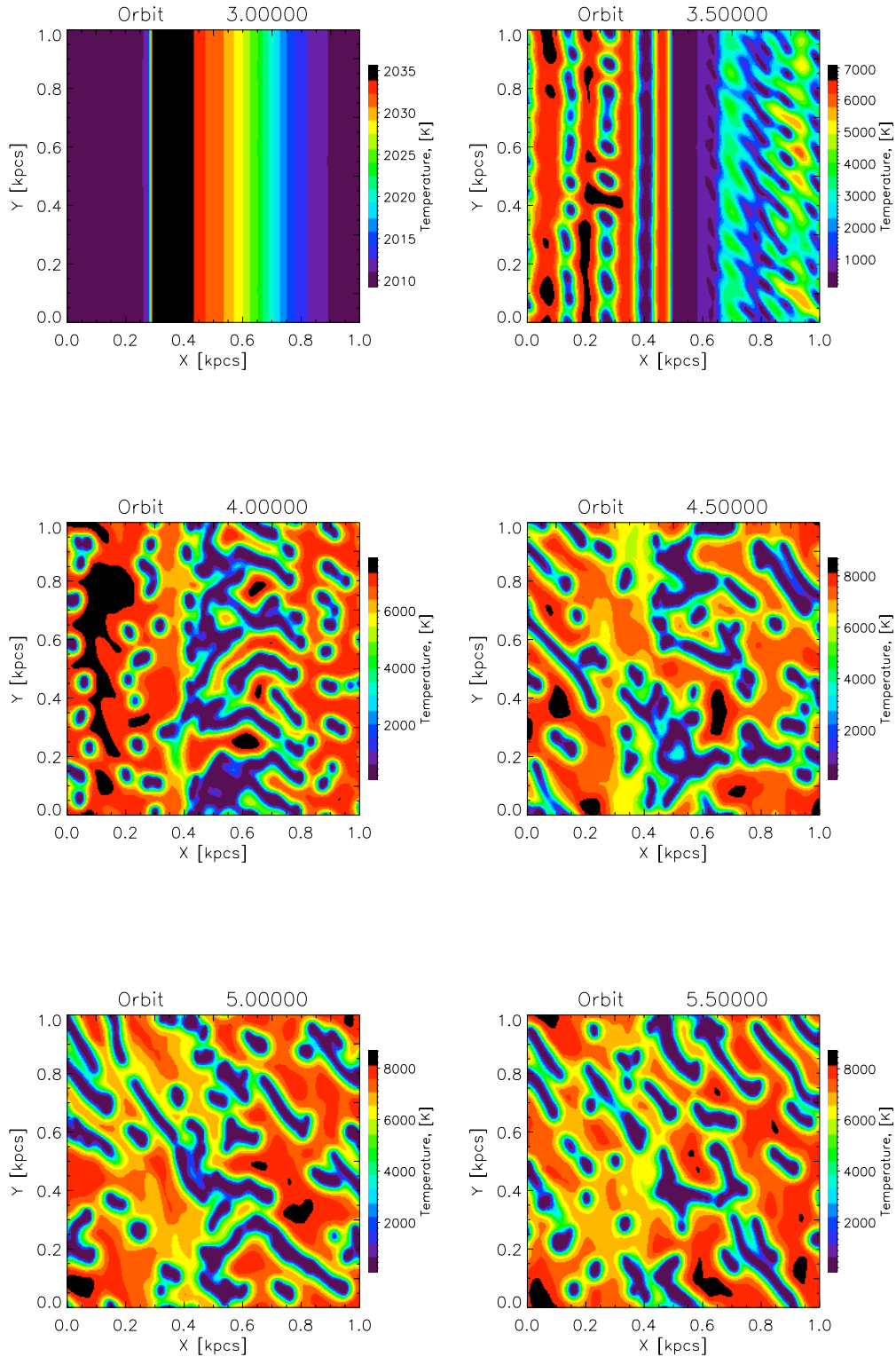


Fig. 23.— Comparison of the time evolution of gas temperature in a sample simulation ($\varepsilon = 0.035$, $\beta = 10$). All the cases considered in this paper have the same general temperature evolution.